Synthesis, Characterisation and Mechanistic Action of Nanomaterials in Stem Cell Therapy

Mihir Iyer[1, 2*], Aadi Mohandas[3]

[1]Interdisciplinary School (IDS) Science, Savitribai Phule Pune University

[2]LCIN Pvt. Ltd.

[3]MIT World Peace University, Pune
*Corresponding Author: *mihiriyer07[at]gmail.com, mihir.iyer[at]learners-club.org*

Abstract: ***Nanomaterial-based strategies have emerged as powerful tools for improving stem cell therapy outcomes in regenerative medicine. This review examines how nanomaterials influence stem cell differentiation, proliferation, and imaging performance through their physicochemical properties and mechanistic interactions with cellular microenvironments. Key classes of nanomaterials, including carbon-based nanostructures, metallic nanoparticles, polymeric carriers, and ceramic scaffolds, are analysed with respect to synthesis, characterisation, and biological activity. Evidence across neurogenic, osteogenic, adipogenic, chondrogenic, and cardiomyogenic differentiation demonstrates that nanoscale surface chemistry, topography, and electrical conductivity modulate lineage commitment through signalling pathways such as MAPK, Wnt, and integrin-mediated cascades. In addition, nanomaterial-assisted imaging techniques enable non-invasive tracking of stem cell fate. Green synthesis approaches and translational considerations are discussed to highlight future clinical prospects. Overall, nanomaterials provide multifunctional platforms that enhance both therapeutic precision and diagnostic capability in stem cell-based interventions.***

Keywords: Stem cell therapy, Regenerative Medicine, Nanobiomaterials, Stem Cell Imaging, Mechanotransduction

1. Introduction

Research on stem cell therapy has increased significantly. The stem cell therapy market is projected to reach an estimated $8.9 billion by 2031 **[1]**. Stem cells are special cells that can completely or partially differentiate and are clonogenic. Thus, stem cells have garnered attention in the field of regenerative medicine. Generally, stem cells are divided into three categories – embryonic stem cells (ESCs), adult stem cells (ASCs) and induced pluripotent stem cells (iPSCs). For successful stem cell therapy, one must explore strategies for selective differentiation and targeted deployment of such differentiated cells. However, to utilize stem cells within regenerative medicine fully, key challenges must be addressed, namely controlled self-renewal, rapid proliferation, and well-defined differentiation **[2]**. To tackle these challenges, nanomaterials provide a unique avenue that is being thoroughly explored.

Nanomaterials are a class of materials that possess unique physical, chemical, optical, and mechanical properties as compared to their bulk counterparts due to their high specific surface area **[3-6]**. Moreover, due to bioorganic, bioinorganic and surface chemical interactions, multiple functionalized NPs can be synthesized. Due to their small size, nanomaterials can mimic extracellular matrix architecture and influence stem cell behaviour **[3, 7, 8]**. The extracellular matrix is a dynamic structure composed of collagen, actin, etc., and signalling molecules that interact and alter cellular functions. Thus, nanomaterials of different chemical compositions, surface topography, mechanical characteristics, electric and magnetic properties, and morphology significantly influence stem cell responses to differentiation **[3, 9-14]**. Nanomaterials are also shown to possess the ability to control stem cell behaviour due to their small size and bioactive behaviour **[3, 9-12]**. Moreover, nanomaterials have extensively been studied for cellular imaging. Cellular imaging allows for the successful identification of transplantable viable stem cells that can integrate with the host tissue and undergo the required differentiation **[2]**. To date, functionalized NPs such as quantum dots (QDs) and magnetic nanoparticles (MNPs), especially superparamagnetic iron oxide nanoparticles (SPIONs) have been utilized for cellular imaging with MRI **[2, 15]**. Thus, combining the effect of nanomaterials on differentiation and utilizing them as contrast agents in imaging proves to be a useful combination which must be extensively studied.

Thus, in this review, we aim to explore such nanomaterials used for selective differentiation and imaging via their mechanism of action, physical properties owing to their synthesis methods, and characterisation of each nanomaterial. We, first, discuss stem cells, their sources, and techniques involved in stem cell therapy. Then, we discuss the nanomaterials utilised within each technique and their mechanism of action. Finally, we discuss green methods to synthesize the discussed nanomaterials.

2. Review Methodology

A comprehensive literature search was conducted across four electronic databases: PubMed/MEDLINE, Scopus, Web of Science, and Google Scholar. The search was conducted between January and October 2024 and covered publications from January 2000 to October 2024 for the primary differentiation and imaging topics, with no date restriction applied to foundational references in materials synthesis and stem cell biology. Seminal papers predating 2000 were identified through backward citation tracking of highly cited review articles and retained where they established key concepts referenced throughout the body of the review, for example, the Turkevich–Frens method for gold nanoparticle synthesis (1951, 1972) and Urist's autoinduction work on bone formation (1965).

Studies were included if they satisfied all of the following criteria: (1) the study investigated the interaction between one or more defined nanomaterials or nanostructured substrates and stem cells of any type, including MSCs, NSCs, adipose-derived stem cells, or induced pluripotent stem cells; (2) the outcome reported included at least one quantified measure of stem cell differentiation or a defined imaging/tracking endpoint; (3) the study was published in a peer-reviewed journal; and (4) the full text was available in English. For the green synthesis sections, inclusion required that the study reported characterisation data for the synthesised nanomaterial such that the identity and morphology of the product could be assessed.

Studies were excluded if they: (1) used cell lines rather than primary stem cells, except in cases where the cell line is a widely accepted model for the relevant differentiation pathway (e.g., MC3T3-E1 pre-osteoblasts for osteogenic differentiation; PC12 cells for neurogenic differentiation), as these have been retained where they provide mechanistic insight directly relevant to the nanomaterial systems reviewed; (2) reported only cytotoxicity or proliferation data without differentiation outcomes; (3) focused exclusively on drug delivery applications of nanomaterials to stem cells without examining differentiation or imaging; or (4) were conference abstracts, preprints, or non-peer-reviewed commentary. Review articles were excluded as primary evidence sources but were used for cross-referencing, contextualisation, and identification of additional primary studies.

Stem Cells

Stem cells possess two unique properties. They differentiate into multiple specialised cell types. They are also clonogenic, i.e., they can proliferate indefinitely to produce the same type of stem cells. They are found in both adult and embryonic organisms but have slightly different properties. Stem cells can be found almost everywhere in the body, distributed in many different organs and tissues including the brain, blood, bone marrow, muscle, skin, heart, and liver tissues.

Many different types of stem cells are present in the human body, each with different functions. They are classified based on their potency and sources **[16]**.

Classification based on potency

Totipotent stem cells possess the ability to differentiate into all types of cells. For example, post-fertilization, the zygote formed is a totipotent stem cell. Pluripotent stem cells possess the ability to differentiate into almost all cell types. The embryonic stem cells emerging from the endoderm, mesoderm and ectoderm germ layers are examples of pluripotent stem cells. Multipotent stem cells possess the ability to differentiate into a closely related family of cells. For example, hematopoietic stem cells are multipotent stem cells that can become RBCs, WBCs or even platelets. Oligopotent stem cells can differentiate into a few cells. A few oligopotent stem cells are adult lymphoid or myeloid stem cells. Unipotent stem cells can only produce cells of their own type. For example, adult muscle stem cells are responsible for the growth, regeneration and repair of skeletal muscle tissue. In clinical use, pluripotent cells are versatile but have higher risks (e.g., tumour formation), while multipotent and oligopotent cells are safer for targeted therapies but have limited application scopes **[16]**.

Classification based on their sources

Categorization of stem cells is also based on their sources i.e. early or embryonic stem cells and mature or adult stem cells. Embryonic stem cells are self-replicating pluripotent cells that are potentially immortal. They are derived from embryos at a developmental stage before the time of implantation would normally occur in the uterus. On the other hand, adult stem cells are undifferentiated totipotent or multipotent cells, found throughout the body after embryonic development, that multiply by cell division to replenish dying cells and regenerate damaged tissues. The primary roles of adult stem cells in a living organism are to maintain and repair the tissues in which they are found **[16]**.

Stem cell therapy

Stem cell therapy is a medical treatment that uses stem cells to repair, replace, or regenerate damaged tissues, cells, or organs. The goal is to leverage the unique regenerative properties of stem cells to treat various diseases, injuries, and disorders. Stem cell therapy can be experimental or approved, depending on the type of stem cells used and the specific medical condition being treated. Stem cell therapy can have multiple approaches and strategies, such as direct stem cell transplantation, paracrine signalling enhancement, immune modulation, and scaffold integration. Stem cell transplantation involves directly transplanting stem cells into the body to replace damaged or diseased cells. Paracrine signalling utilises stem cells for their ability to secrete growth factors, cytokines, and extracellular vesicles that promote healing and reduce inflammation. Genetically modified stem cells open another avenue within stem cell therapy. They can be designed using CRISPR technology. These genetically engineered stem cells are also sometimes used to enhance their therapeutic potential or correct genetic defects. A less extensively studied approach is to combine stem cells with biocompatible scaffolds to create engineered tissues that can be implanted **[17]**.

Nanomaterials provide an edge to aid the abovementioned strategies. Due to their small size, nanomaterials express different physicochemical properties and biological activity than their bulk counterparts. Thus, nanomaterials have been used in various technological applications, cosmetics, paints, textiles, and optical and electronic devices. Nanomaterials, when placed in a biological environment, are exposed to different biomolecules, exosomes and whole cells **[18]** to which they can adhere via covalent interactions, van der Waal's forces, hydrophobic interactions, electrostatic interactions, and more. Hence, nanomaterials can alter the cell signalling pathways that govern stem cell therapy.

Nanomaterial-aided Stem Cell Differentiation

Stem cell differentiation can be directed towards any desired lineage by providing an environment suitable for the synthesis and expression of growth factors. Nanomaterials enhance this process via various mechanisms discussed ahead.

Neurogenic Differentiation

Neural stem cells (NSCs) are a source of various cell types. They are a subpopulation of cells that can self-renew and give rise to identical daughter cells. They are multipotent, capable of generating diverse neural lineages, encompassing neurons, astrocytes, and oligodendrocytes **[19]**. Neurogenic differentiation takes place during both embryonic development and adult stages of life. During embryonic development, neurogenic differentiation is crucial for forming the nervous system. The differentiation occurs during the neural induction phase, where the cells in the neural plate, differentiate into neural progenitors, which are precursor cells that can further develop into different types of neurons and glial cells. Neural progenitors include neuroepithelial cells, radial glial cells, intermediate progenitor cells, neural crest cells and glioblasts. These progenitors play critical roles in developing the brain, spinal cord, and peripheral nervous system during embryogenesis **[19].** On the other hand, adult neurogenesis takes place in the hippocampus and the subventricular zone. This process allows the generation of new neurons, involved in learning, memory, and repairing damaged neural tissue. Adult neurogenesis can be stimulated naturally by factors like brain injury, exercise, enriched environments, and certain pharmacological agents like fluoxetine, sertraline, valproic acid, N-acetylcysteine and resveratrol **[19].**

These growth factors and chemical agents are the most common signals to promote the proliferation and differentiation of stem cells. However, the stimulation of stem cell differentiation by using growth factors and chemical agents is unstable, inefficient, and hazardous. To address these limitations, nanomaterials have been recently used to control stem cell growth and differentiation **[20].** A study by Halim et al. **[20]**, showed that graphene (Gp), a 2D carbon-based nanomaterial containing a single layer of carbon atoms packed in a honeycomb crystal lattice with sp^2 hybridisation, and its derivatives, graphene oxide (GO), and reduced graphene oxide (rGO) have been shown to influence the self-renewal and differentiation of stem cells **[20]**. Particularly, rGO has been shown to enhance neurogenesis due to the recovery of its electrical conductivity following the removal of oxygen-containing groups from GO **[20]**. However, several reports are showing that GO could also enhance the differentiation of NSCs even better than rGO, which might be due to the surface hydrophilicity of GO **[20]**. Studies have shown that rGO, both as a standalone material and in hybrid composites, can potentially promote NSC differentiation towards neurons, characterised by the elevation of Tuj1 and MAP2 expression levels **[20]**.

Various nanomaterials and nanostructures have been utilised for this purpose. Tay et al. synthesized carboxylated SWCNT films to examine the behaviour of hMSCs without a specific differentiating medium **[21]**. MSCs spread and proliferated on SWCNT films, and neurogenic markers were upregulated while osteogenic markers remained low. Another study by Kam et al. examined the effects of SWCNTs coupled with laminin films on hMSCs. Laminin-SWCNT films demonstrated better growth and proliferation of neural stem cells and triggered longer outgrowths than pure laminin substrates **[22]**. Moreover, synthesizing laminin-SWCNT composites layer-by-layer promotes adhesion, differentiation, and mediates electrical stimulation of neuronal cell lines. The physical properties of this composite potentially allow for spontaneous differentiation, as evidenced by the presence of differentiated neuron and glial cell protein markers (microtubule-associated protein 2, glial fibrillary acidic protein) **[22]**.

MSCs cultured with Au-decorated GO nanocomposites for 7 days showed significant upregulation of neuron markers, as reported by Hung et al. **[23]**. On evaluation of the SDF-1/CXCR4 axis activation, both GO-Au and GO-Au (×2, i.e., coated twice) showed an upregulation of 6.7x and 6.9x respectively, as compared to the control group (1.8x). On culturing the MSCs in media with the nanomaterial and subsequent exposure to specific markers associated with neurogenic differentiation, it was observed that neuron markers such as nestin, GFAP, and β-tubulin were significantly increased 7.0-, 13-, and 5Liu.7-fold, in GO-Au (×2); increased 4.3-, 7.1-, and 5-fold in GO-Au; and increased 2.3-, 2.3-, and 3.3-fold in GO, respectively **[23]**.

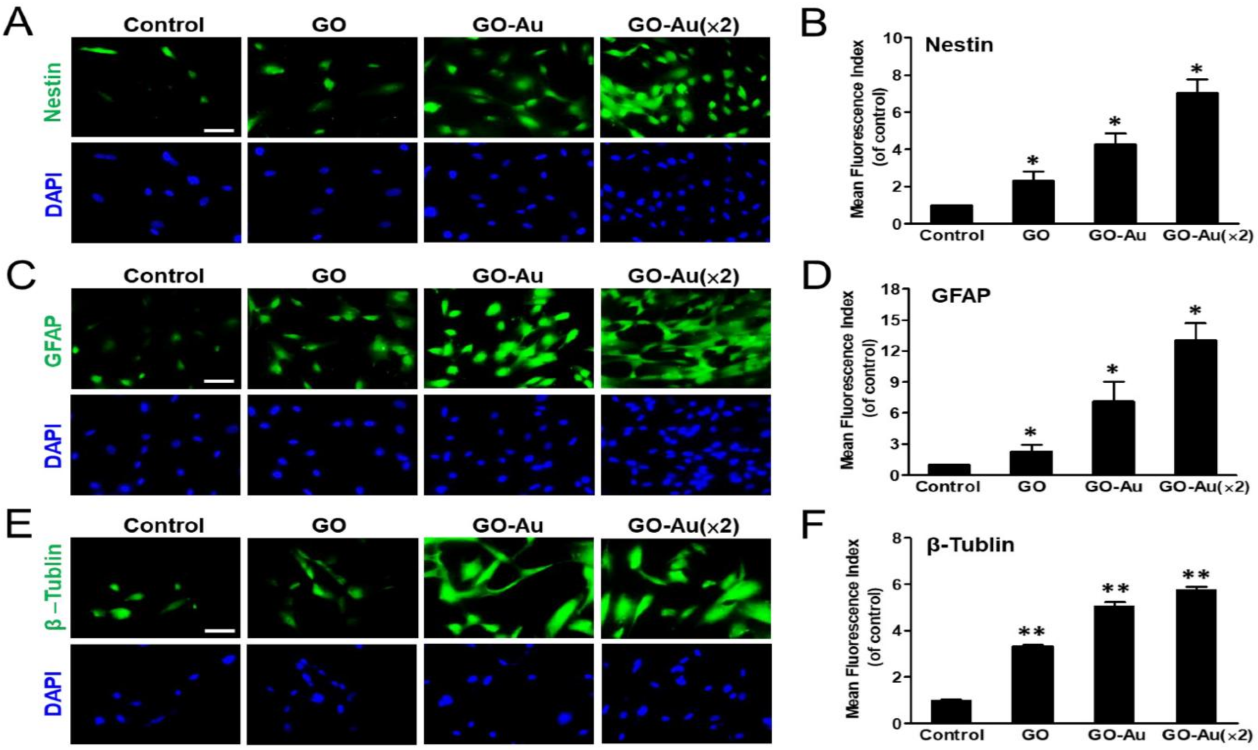

Figure 1: Characterization of GO-Au-mediated MSC differentiation into neuron cells. Cells were cultured on various nanomaterials of GO, GO-Au, and GO-Au (×2) for 7 days. Then, cells were analyzed for expression levels of (A, B) nestin, (C, D) GFAP and (E, F) β-tubulin protein expression. Data were presented as the mean ± SD, * $p < 0.05$ and ** $p < 0.01$. Reproduced under CC BY 4.0 from **[23]**

Differentiation and proliferation of hMSCs were studied on PDMS nanogratings of 350 nm width **[24]**. Cytoskeleton and nuclei of hMSCs were aligned and elongated along the nanogratings, and gene profiling and immunostaining showed significant upregulation of neuronal markers such as microtubule-associated protein 2 (MAP2), compared to unpatterned and micropatterned controls. The combination of nanotopography and biochemical cues such as retinoic acid further enhanced neuronal marker expression, but nanotopography alone showed a stronger effect compared to retinoic acid on unpatterned surfaces **[24]**. Three-dimensional nanostructured microarchitectures were reported to strongly promote cell alignment and efficient neurogenic differentiation, where over 85% of hMSCs expressed MAP2, a mature neuronal marker, after just 7 days of culture on the nanostructured surface. This is a particularly striking result given the high conversion efficiency without chemical induction media **[25]**.

Baranes et al. demonstrated that gold nanoparticle-decorated scaffolds promote neuronal differentiation and maturation **[26]**. Their results show that the nanocomposite scaffolds have encouraged a longer outgrowth of the neurites, as judged by the total length of the branching trees and the length and total distance of neurites. Moreover, neurons grown on the nanocomposite scaffolds had fewer neurites originating out of the soma and lower number of branches. These findings indicate that neurons cultivated on the gold nanoparticle scaffolds prefer axonal elongation over forming complex branching trees **[26]**. Separately, Bhang and coworkers showed that MnAu nanoparticles enabled cellular neuronal differentiation without cellular toxicity through a pH-triggered release of manganese **[27]**. This is done by utilising the different reduction potentials of Au and Mn. Compared to PC12 cells treated with a high concentration of free Mn^{2+}, PC12 cells treated with an equal concentration of MnAuNPs resulted in significantly enhanced cellular neurodevelopment with decreased apoptosis and necrosis. Gold nanoparticles thus act both as structural scaffold components and as signaling modulators for neurogenic fate.

Table *1* lists a summary of the nanomaterials discussed in the application of neurogenic differentiation.

Table 1: List of nanomaterials used for neurogenic differentiation, key neurogenic markers upregulated, and relevant stem cell or cell types

Nanomaterial	Particle Size (nm)	Stem Cell Type	Key Neurogenic Markers / Observations	Reference
Carboxylated SWCNT films	~1–2 (diameter)	hMSCs	Upregulation of neurogenic marker genes; osteogenic markers remained low. Differentiation attributed to nanotopography of SWCNT film.	[21]
Laminin–SWCNT composite films (layer-by-layer)	~1–2 (diameter)	Neural stem cells / neuronal cell lines	Enhanced growth, proliferation, and longer neurite outgrowths vs. pure laminin. Expression of MAP2 and GFAP confirmed spontaneous neural and glial differentiation.	[22]

Graphene oxide (GO)	Lateral: variable (sheet)	hMSCs	Nestin ↑ 2.3×, GFAP ↑ 2.3×, β-tubulin ↑ 3.3× vs. control. Activation of SDF-1/CXCR4 axis (1.8× vs. control).	[23]
GO–Au nanocomposite (GO-Au)	Au NPs: ~15–30 on GO sheet	hMSCs	Nestin ↑ 4.3×, GFAP ↑ 7.1×, β-tubulin ↑ 5.0×. SDF-1/CXCR4 axis upregulation: 6.7×.	[23]
GO–Au nanocomposite, double-coated (GO-Au ×2)	Au NPs: ~15–30 on GO sheet	hMSCs	Nestin ↑ 7.0×, GFAP ↑ 13×, β-tubulin ↑ 5.7×. Highest neurogenic marker expression across all GO-based groups. SDF-1/CXCR4 axis: 6.9×.	[23]
PDMS nanogratings	350 nm (grating width)	hMSCs	Cytoskeletal and nuclear elongation along grating axis. Significant MAP2 upregulation vs. unpatterned and micropatterned controls. Nanotopography alone outperformed retinoic acid on unpatterned surfaces.	[24]
3D nanostructured microarchitectures	Nanostructured features; scaffold-scale construct	hMSCs	>85% of cells expressed MAP2 (mature neuronal marker) after 7 days in the absence of chemical induction media. Differentiation driven by mechanotransduction.	[25]
Gold nanoparticle (AuNP)-decorated scaffolds	~20–50	Neurons (primary)	Promoted neuronal differentiation and maturation. Longer total neurite outgrowth; preference for axonal elongation over branching. Fewer neurites per soma on AuNP scaffolds.	[26]
Manganese–gold bimetallic nanoparticles (MnAuNPs)	~30–60	PC12 cells	pH-triggered Mn^{2+} release enabled neuronal differentiation without cytotoxicity. Significantly enhanced neurodevelopment with decreased apoptosis and necrosis vs. free Mn^{2+} at equal concentration.	[27]

Osteogenic Differentiation (Mihir)

Osteoblasts are the building blocks of bone structures. Bone tissues are a nanocomposite of collagen fibrils and hydroxyapatite plates. Despite being mineralised, they are dynamic and especially active during the growth stages of an organism. To accommodate the shape of the skeleton in each stage of growth, a process called bone modelling takes place. If bone modelling fails, usually due to genetic diseases or severe malnutrition, the consequences are highly disabling at best, but more often fatal in infancy if not treated **[28]**. Thus, the bone needs to be deposited and resorbed continuously at different locations for bone modelling to be successful. Two types of specialised cells are involved in this: osteoblasts and osteoclasts. During bone modelling, osteoblasts must produce more bone than what osteoclasts resorb since the organism is still growing, and therefore, the net result of bone modelling is bone accrual **[29-31].**

Osteoblasts derive from MSCs that reside within the bone marrow. Differentiation of MSCs towards the osteogenic line is tightly controlled by bone morphogenic proteins (BMPs) **[29, 32-34]** and wingless-related integration site (WNT) pathways **[29, 35-39]**. However, other pathways, namely that of nuclear factor κB and NAD+-dependent deacetylase sirtuin-1 are also observed **[29]**. Differentiation begins with a commitment to a common osteo-chondroprogenitor cell, which undergoes further commitment upon activating key osteogenic transcription factors like RUNX2, OSX, and DLX5. This committed cell transitions to a pre-osteoblast through the transcription of early osteogenic genes including ALP and COL1A1, along with sustained expression of osteoblast markers like osteopontin (OPN), bone sialoprotein (BSP II), and osteocalcin (OCN). **[29, 40]**.

In recent years, multiple reports of various nanomaterials have demonstrated an osteogenic line bias for stem cell differentiation. A study by Liu et al. **[41]** demonstrated that spherical hydroxyapatite-PLGA nanocomposite (HAP-PLGA) scaffolds in MSCs grown in an osteogenic medium possess high cell adhesion, proliferation and differentiation. This was supported by studying the calcium deposition of the MSCs. More interestingly, the same study compared the performance of a short peptide sequence derived from BMP-7, a potent osteogenic growth factor, and showed that it produced results comparable to the HAP-PLGA nanocomposites as the HAP-PLGA nanocomposites and the HAP-PLGA-peptide nanocomposites **[41]**. These results can be attributed to nanoscale surface features of HAP-PLGA nanocomposites. These provide an ideal surface for cell adhesion and physical adsorption of serum molecules in the osteogenic medium. In comparison, another study by Mahmoud et al. **[42]** studied HAP-NPs with a rod-like shape. It revealed that the presence of the NPs created no significant changes within the proliferation or other cell behaviours. However, it showed an insignificant impact on the gene expression levels of Runx-2 and BMP-2 genes, used to check for osteogenic differentiation in MSCs, by increasing it by 1.2 times. As documented by Yuan et al. **[43]**, a possible reason for this is the action of HAP, modifying MSC microenvironments since HAP NPs act through adsorbing proteins to form a neo-matrix **[42]**.

The same study **[42]** reported using spherical gold nanoparticles (AuNPs). The gene upregulation of Runx-2 and BMP-2 genes was increased by 4.9 times. This result was corroborated by Yi et al. **[44]**, who explained it by supposing that AuNPs interact with the cell membrane and enter the cell via receptor-mediated endocytosis, binding to the cytoplasmic proteins, leading the cells to osteogenic differentiation by activating the p38 MAPK pathway, causing the upregulation of Runx-2 **[45]**, followed by the upregulation of Col-1a and BMP-2 at the early stages of differentiation **[46]**. Incubating MSCs in an osteogenic medium with NPs leads to the adsorption of serum proteins to their surface and causes their entry into the cell via endocytosis **[47, 48]**. These proteins interfere with the ERK signalling axis, essential for osteogenic differentiation **[49]**.

A study by Lee et al. **[50]** investigated the effects of selenium nanoparticles (SeNPs). The osterix and ALP gene proliferation levels after 3 days were as follows: negative control 1.00 ± 0.05, positive control 1.19 ± 0.06, 5 μg/mL 1.47 ± 0.03, 10 μg/mL 1.47 ± 0.13, and 20 μg/mL 1.51 ± 0.03 for osterix. For ALP, the values were as follows: negative control 1.00 ± 0.01, positive control 2.41 ± 0.04, SeNPs at 5 μg/mL 3.40 ± 0.09, SeNPs at 10 μg/mL 3.48 ± 0.04, and SeNPs at 20 μg/mL 3.33 ± 0.07. **[50]**. After 7 days, a notable increase was observed in osterix levels. The negative control group had a value of 1.00 ± 0.14, the positive control was 1.32 ± 0.02, and SeNPs at 5 μg/mL, 10 μg/mL, and 20 μg/mL had values of 1.60 ± 0.13, 1.45 ± 0.04, and 1.05 ± 0.01, respectively. In terms of ALP expression, the negative control group showed a value of 1.00 ± 0.01, the positive control was 2.19 ± 0.66, and SeNPs at 5 μg/mL, 10 μg/mL, and 20 μg/mL displayed values of 2.86 ± 0.08, 2.75 ± 0.05, and 2.55 ± 0.15, respectively **[50]**. ALP staining was performed to confirm osteogenic differentiation, which showed better results in cells treated with SeNPs and osteogenic differentiation medium than in cells only treated with osteogenic differentiation medium (ODM). To confirm the level of differentiation, ARS staining was performed, which showed significant mineralisation in cells treated with 5-10 μg/mL SeNPs and grown in ODM than cells grown in only ODM. Moreover, the degree of calcification in the H2O2-treated group is insignificant compared to the untreated group. This indicates that SeNPs promote the early stages of differentiation.

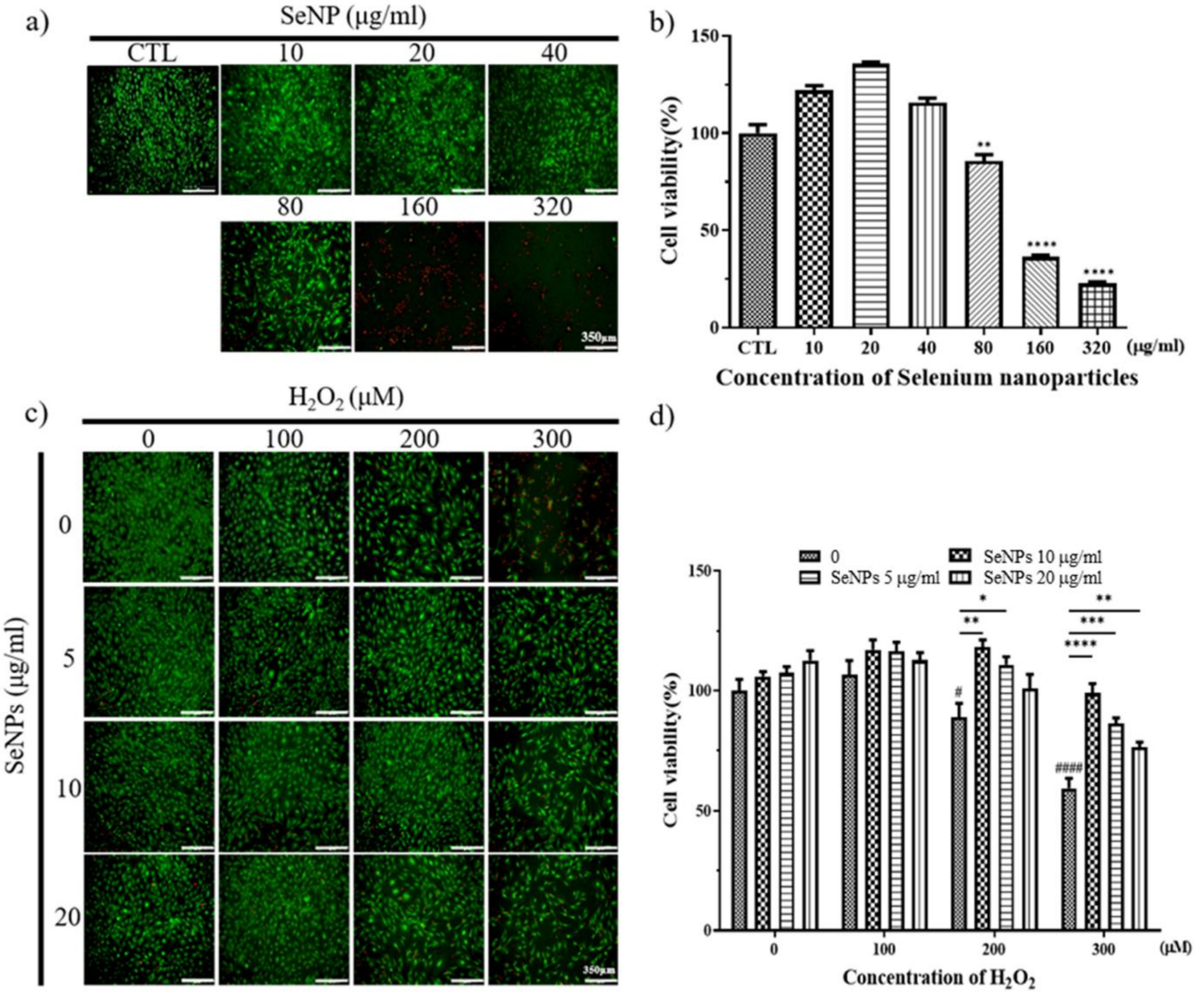

Figure 2: Cell viability and proliferation were determined by live (green) and dead (red) and CCK-8 assays. After cell seeding for 24 h, MC3T3-E1 cells were analyzed using CCK-8 solution and stained using live and dead staining to evaluate cell viability. (a) Live and dead staining following treatment with various SeNP concentrations. (**b**) The relative cell viability of MC3T3-E1 cells cultured in different concentrations of SeNPs. (**c**) Live and dead staining following treatment with various SeNP concentrations and H_2O_2. (**d**) Cell viability of MC3T3-E1 cells treated with various concentrations of SeNPs and H_2O_2. The statistical significance of (b) was calculated using one-way analysis of variance (ANOVA), and (d) was calculated using two-way ANOVA followed by a two-sided Dunnett's multiple comparison test compared to control (CTL) (scale bar = 350 μm). * Represents $p < 0.05$, ** $p < 0.01$, *** $p < 0.001$, **** $p < 0.0001$, $^{\#}$ is compared with SeNPs and H_2O_2-untreated groups. $^{\#}$ Represents $p < 0.05$, $^{\#\#\#\#}$ $p < 0.0001$; n = 4. Reproduced under CC BY 4.0 from **[50]**

Xia et al. **[51]** showed the increased efficacy of Zn-based carbon nano scaffolds towards osteogenic differentiation. Carbon nanomaterials are reported to provide binding sites with high stiffness to cell membrane receptors, and large adsorption and accumulation of nutrients **[51-53]**. This promotes the rapid formation of focal adhesions. This leads to F-actin rearrangement, YAP signal translocation, increased Lamin A/C expression, activation of RUNX-2, and enhanced osteogenic differentiation **[54-55]**. To test this, they incorporated carbonised ZnO nanostructures into poly(ε-caprolactone) (PCL) nanofibers (PCL-C-ZnO). To compare, they performed all tests with only ZnO incorporated into PCL

(PCL-ZnO) and pure PCL. ALP activity was the highest in PCL-C-ZnO and the activity of PCL-ZnO and PCL were comparable. Similar results were observed for IBSP staining. They also observed high YAP signal translocation up to two times that of PCL. On immunofluorescence staining, they observed linear f-actin microfilaments with higher vinculin expression on PCL-C-ZnO indicating that the carbon nanomaterials have provided more binding sites for focal adhesions. Moreover, PCL-C-ZnO also exhibited increased Lamin A/C expression, RUNX2 signal and higher bacterial inhibition. Thus, this material is a promising candidate to induce the early stages of osteogenic differentiation, supported by the enhanced expression of pre-osteogenic biomarker RUNX2.

Many nanomaterials also show an immunomodulative mechanism of osteogenic differentiation, owing to their surface chemistry, physical properties, and structural effects. Previous studies indicate low macrophage and foreign body giant cell formation, enhancing osteointegration of implants due to the hydrophilic surface of NMs as compared to hydrophobic surfaces **[56]**. For example, Mendonça et al. synthesised modified Ti disks, providing hydrophilicity by fabricating them in an N_2 atmosphere and storing them in an isotonic solution at pH 4-6 **[56]**. TGF-b/BMP signalling was upregulated with the promotion of osteoblasts on hydrophilic substrates. The hydrophilic Ti surface also significantly stimulated macrophage polarisation toward the healing-associated M2 type by increasing IL-10 secretion and reducing pro-inflammatory factors like IL-1b, IL-6, and IL-8 **[57]**. Similarly, Brodbeck et al. **[58]** prepared functionalised acrylamide materials with an anionic functional group of poly(acrylic acid) which promoted the expression of the anti-inflammatory factor IL-10 and inhibited the expression of the pro-inflammatory factor IL-8. Further analysis revealed that the hydrophilic and anionic surfaces inhibited monocyte adhesion and IL–4-mediated macrophage fusion into foreign body giant cells (FBGCs), further cementing its anti-inflammatory activity **[58]**.

Physical properties like topography, roughness, porosity and, in extension, pore size influence osteogenesis **[59]**. Huang et al. **[60]** fabricated a Cu-containing nanotopographical bioceramic surface. They observed that the nanotopographical substrate played a small anti-inflammatory role, contrary to the pro-inflammatory role of Cu, via the upregulation of integrin and TLR signalling **[60]**. Similarly, roughness also influences adhesion, proliferation and differentiation of osteoblasts, as evidenced by Ma et al. **[61]**. They prepared TiO_2 surfaces with varying roughness to investigate the effect of different nanoroughness groups on osteoimmunomodulation. Surfaces with higher roughness showed a more pro-inflammatory immune response **[61]**. However, the mechanisms of action towards immune cells is not well understood.

Changing the morphology of nanomaterials also affects their immunomodulation capacity. Bordoni et al. fabricated a bioactive material by combining graphene oxide (GO) and calcium phosphate (CaP) with a nanoscale lateral dimension **[62]**. This 1D nanomaterial evoked the activation of monocytes and increased the expression of osteogenic markers by upregulating BMP and Wnt signalling **[62]**. Moreover, 2D nanomaterials provide unique nanotopography which, as previously discussed, contributes significantly to osteoimmunomodulation. 3D nanomaterials fabricated based on 1D and 2D morphologies can mimic bone architecture which can provide multiple mechanical and immunological cues to improve osteogenesis. Song et al. **[59]** fabricated a hierarchal zinc silicate/nanohydroxyapatite/collagen material by the robocasting method. These scaffolds with 10% Zn could stimulate the differentiation of monocytes via the p38 pathway to tartrate-resistant acid phosphatase (TRAP)-positive cells which recruit BMSCs and endothelial cells to bone-defect areas **[59]**. Table 2 lists various nanomaterials being used

Table 2: List of nanomaterials used for osteogenic differentiation, key osteogenic markers and observations, and relevant stem cell or cell types

Nanomaterial	Particle Size (nm)	Stem Cell / Cell Type	Key Osteogenic Markers / Observations	Reference
HAP–PLGA nanocomposite (spherical)	36	MSCs (osteogenic medium)	High cell adhesion, proliferation, and differentiation. Calcium deposition comparable to BMP-7 short peptide and HAP-PLGA-peptide composites. Nanostructured surface promotes focal adhesion and serum protein adsorption.	[41]
HAP nanoparticles (rod-like)	80–125.4 (length) 35–45.7 (width)	MSCs	Runx-2 and BMP-2 gene expression increased 1.2×. No significant change in cell proliferation or behaviour. HAP acts via neo-matrix formation through adsorbed protein layer on NP surface.	[42]
Gold nanoparticles (AuNPs, spherical)	30.2–40.7	MSCs	Runx-2 and BMP-2 gene expression increased 4.9×. Mechanism: receptor-mediated endocytosis → p38 MAPK pathway activation → Runx-2 upregulation → Col-1a and BMP-2 expression at early differentiation stages.	[42]
Au–HAP nanoparticles	11.4–22.0 (width) 38.5–97.9 (length)	MSCs	Combined osteogenic effect of AuNP (p38 MAPK) and HAP (neo-matrix) mechanisms. Adsorption of serum proteins to NP surface interferes with ERK signalling axis essential for osteogenic differentiation.	[42]
Chitosan (CT) nanoparticles	35.8–64.3	MSCs	Biocompatible polymeric NPs supporting MSC adhesion and osteogenic commitment. Surface electrostatic interactions facilitate serum protein adsorption relevant to osteogenic induction.	[42]
Chitosan–HAP (CT-HAP) nanoparticles	20.0–122.6	MSCs	Composite NPs combining the biocompatibility of chitosan with the osteoconductive properties of HAP. Promotes MSC osteogenic commitment through combined surface chemistry and neo-matrix formation.	[42]

Selenium nanoparticles (SeNPs)	~25.3	MC3T3-E1 pre-osteoblasts	Osterix and ALP upregulated at days 3 and 7 (ALP: 3.40 ± 0.09 at 5 µg/mL vs. 2.41 ± 0.04 positive control, day 3). ALP and ARS staining confirmed early mineralisation at 5–10 µg/mL, including under oxidative stress (H_2O_2). SeNPs promote the early stages of differentiation.	[50]
Carbonised ZnO in PCL nanofibers (PCL-C-ZnO)	C-ZnO: ~50	MSCs	Highest ALP activity across PCL, PCL-ZnO, and PCL-C-ZnO groups. YAP signal translocation 2× vs. PCL. F-actin rearrangement with higher vinculin expression confirming focal adhesion formation. RUNX2 and Lamin A/C expression increased. IBSP staining positive. Enhanced bacterial inhibition.	[51]
Hydrophilic titanium surface (modified Ti disks)	Nanoscale surface features	Macrophages / osteoblasts	TGF-β/BMP signalling upregulated promoting osteoblast activity. Macrophage polarisation toward anti-inflammatory M2 type: IL-10 secretion increased; IL-1β, IL-6, and IL-8 decreased. Immunomodulatory mechanism of osteogenesis.	[56]
Anionic poly(acrylic acid) acrylamide surface	Polymer coating	Monocytes / macrophages	IL-10 (anti-inflammatory) expression promoted; IL-8 (pro-inflammatory) inhibited. Inhibited monocyte adhesion and IL-4-mediated macrophage fusion into foreign body giant cells (FBGCs). Anti-inflammatory surface drives immunomodulatory osteogenesis.	[58]
Cu-containing nanotopographical bioceramic surface	Nanotopographical features	Macrophages / osteoblasts	Nanotopographical substrate played an anti-inflammatory role via upregulation of integrin and TLR signalling, counteracting the pro-inflammatory effect of Cu. Dual biophysical and chemical modulation of osteoimmunomodulation.	[60]
TiO_2 nanostructured surfaces (varying roughness)	Nanoscale roughness groups	Macrophages / BMSCs	Higher surface roughness → more pro-inflammatory immune response. Macrophage-mediated cytokine secretion (sRANKL/OPG/M-CSF) from BMSCs on nanostructured Ti influenced osteogenesis. Mechanistic basis of surface roughness on osteoimmunomodulation.	[61]
Graphene oxide–calcium phosphate (GO-CaP, 1D nanomaterial)	Nanoscale lateral dimension	Monocytes / osteoblasts	Activated monocytes and increased expression of osteogenic markers via upregulation of BMP and Wnt signalling. 1D nanomaterial morphology evoked selective monocyte activation. In vivo bone formation confirmed.	[62]
Zinc silicate / nanohydroxyapatite / collagen scaffold (10% Zn, robocasting)	Hierarchical 3D architecture	Monocytes / BMSCs / endothelial cells	10% Zn stimulated monocyte differentiation via p38 pathway into TRAP-positive cells, recruiting BMSCs and endothelial cells to bone-defect areas. Hierarchical 3D architecture mimics native bone. Immunomodulatory route to osteogenesis.	[59]

Adipogenic Differentiation

Adipogenic differentiation of MSCs produces adipocytes, the primary cellular constituents of adipose tissue. Adipocytes are metabolically active cells responsible for lipid storage, thermogenesis, and the secretion of adipokines, which include adiponectin, leptin, and resistin, modulating systemic metabolic homeostasis and immune function **[63]**. Maladaptive adipogenesis is implicated in several conditions relevant to regenerative medicine, including obesity-induced bone marrow adiposity, which competes with osteogenesis for MSC commitment and impairs haematopoiesis. Conversely, directed adipogenic differentiation of MSCs is actively explored for soft tissue engineering, lipodystrophy treatment, and fat-graft augmentation strategies **[63]**.

Adipogenesis proceeds through two sequential stages: the commitment of MSCs to a preadipocyte fate, followed by terminal differentiation of preadipocytes into mature, lipid-laden adipocytes. The process is tightly regulated by two master transcription factors; (1) peroxisome proliferator-activated receptor gamma (PPARγ) and (2) CCAAT/enhancer-binding protein alpha (C/EBPα); which act in concert to activate the adipogenic gene programme **[63]**. Early-stage initiators include C/EBPβ and C/EBPδ, which are rapidly induced by conventional chemical inducers such as isobutylmethylxanthine (IBMX), dexamethasone (DEX), insulin, and indomethacin. IBMX inhibits phosphodiesterases, raising intracellular cyclic AMP (cAMP) levels and activating protein kinase A, which in turn triggers the downstream transcriptional cascade culminating in PPARγ and C/EBPα activation **[63]**. The principal assays used to confirm adipogenic differentiation are Oil Red O (ORO) staining for cytoplasmic lipid vacuoles and triglyceride content measurement, along with gene and protein expression analysis of PPARγ, C/EBPα, fatty acid-binding protein 4 (FABP4), lipoprotein lipase (LPL), and adiponectin **[64]**.

Several nanomaterials and nanostructured substrates have been shown to modulate this pathway, either by enhancing adipogenic marker expression in the presence of chemical induction media, or, in fewer cases, by influencing lineage commitment in the absence of exogenous chemical inducers. The mechanisms involved are diverse, spanning nanotopography-driven cytoskeletal changes, reactive oxygen species (ROS)-mediated signalling, and direct gene delivery via nanoscale vectors.

Lee et al. **[64]** performed a systematic comparison of MSC behaviour on three substrates: polydimethylsiloxane (PDMS), graphene (G), and graphene oxide (GO), under identical adipogenic induction conditions. After 14 days, Oil Red O staining revealed a significantly greater accumulation of cytoplasmic lipid vacuoles in MSCs cultured on GO than in those on either G or PDMS ($p < 0.05$; $n = 4$). No lipid deposition was observed in any group in the absence of chemical inducers, establishing that GO acts as an enhancer of chemically-directed adipogenesis rather than a standalone inducer. The superior adipogenic response on GO compared to pristine graphene was attributed to the oxygen-containing functional groups on GO, primarily epoxide, hydroxyl, and carboxyl moieties, which confer surface hydrophilicity, promote selective adsorption of serum proteins and growth factors, and increase the interaction surface between the substrate and the cell membrane. This is consistent with the general principle observed in the osteogenic section, where surface chemistry and hydrophilicity significantly influence MSC lineage commitment **[56]**.

The role of silver nanoparticles in adipogenic differentiation was investigated by Tung et al. **[65]**, who fabricated AgNP-decorated surfaces via plasma polymerization and examined their effect on human bone marrow-derived MSCs. The AgNP-coated surfaces did not adversely affect initial cell adhesion, spreading, or proliferation. However, under adipogenic induction conditions, AgNP-coated surfaces produced markedly greater lipid droplet accumulation than uncoated controls, accompanied by upregulation of PPARγ, adipocyte determination and differentiation factor 1 (ADD1/SREBP1c), and C/EBPα at the gene expression level. Critically, the study showed that AgNPs caused a dose-dependent accumulation of intracellular ROS in MSCs undergoing adipogenic induction, and that the activation of antioxidant enzyme expression was positively correlated with enhanced adipogenic capacity **[65]**. This ROS-mediated mechanism is significant because it draws a mechanistic parallel to the osteogenic inhibition reported in the same system. The divergence between adipogenic and osteogenic outcomes appears to depend on the magnitude and duration of ROS signalling, rather than its mere presence.

This ROS-adipogenesis connection was independently corroborated by Kim et al. **[66]**, who studied the effects of gold nanostructures on the differentiation of bone marrow-derived MSCs (bMSCs). They compared spherical AuNPs and 11-mercaptoundecanoic acid (MUA)-functionalised gold nano-octahedra (MUA-AuNOs) at concentrations of 5 μg mL^{-1} and 25 μg mL^{-1}. Both nanostructures enhanced adipogenic differentiation as evidenced by Oil Red O staining, and upregulated PPARγ and FABP4 at both mRNA and protein levels. Importantly, the effects were both structure- and dose-dependent: MUA-AuNOs were more effective than spherical AuNPs at promoting adipogenesis, an outcome the authors attributed to the higher levels of ROS generated by the anisotropic nano-octahedral geometry and MUA surface functionalization **[66]**. Concurrently, alkaline phosphatase activity and Alizarin Red S staining indicated a weakened osteogenic potential in the same treated cells, suggesting that the nanostructures shifted MSC lineage commitment away from osteogenesis and towards adipogenesis. This is consistent with the well-established osteogenic–adipogenic reciprocity in MSC fate decisions, wherein activation of PPARγ suppresses the osteogenic master regulator RUNX2 **[29, 63]**.

The importance of surface ligand density, and by extension, integrin signalling, in governing adipogenic outcomes was demonstrated by Zhao et al. **[67]**, who synthesized RGD (arginine-glycine-aspartate)-modified AuNPs with tunable surface ligand densities to mimic ECM-receptor interactions. The biomimetic NPs were taken up by hMSCs in a ligand density-dependent manner, confirmed by TEM and confocal imaging. When cultured in adipogenic induction medium, MSCs treated with high-RGD-density AuNPs showed promoted oil droplet formation and upregulated adipogenic marker gene expression, whereas low-RGD-density AuNPs exerted an inhibitory effect. The mechanistic basis was traced to differential focal adhesion formation and cytoskeletal tension: high ligand density AuNPs facilitated extensive integrin clustering, promoting a rounded, low-tension cytoskeletal configuration consistent with adipogenic commitment, while low ligand density NPs maintained the spread, high-tension morphology associated with osteogenic fate **[67]**. This study highlights that the surface chemistry of AuNPs is also a critical determinant of adipogenic versus osteogenic lineage outcomes.

A distinct approach to adipogenic differentiation was reported by Kim et al. **[68]**, who employed poly(ethyleneimine)-coupled PLGA nanospheres (PEI-PLGA) as vectors to deliver the adipogenic transcription factors C/EBPα and C/EBPβ directly into hMSCs. C/EBPα and C/EBPβ, fused to green fluorescent protein (GFP) and red fluorescent protein (RFP) respectively, were complexed with PEI and encapsulated within the PLGA nanospheres. FACS analysis confirmed transfection efficiencies of 12.59% for C/EBPα alone, 21.74% for C/EBPβ alone, and 28.96% for co-delivery of both transcription factors. Expression and nuclear localisation of the delivered proteins were confirmed by Western blotting and confocal laser scanning microscopy. Overexpression of exogenous C/EBPα and C/EBPβ significantly elevated adipogenic differentiation, as evidenced by RT-PCR, real-time PCR, Western blotting, histology, and Oil Red O staining **[68]**. This gene delivery approach is conceptually distinct from the substrate and nanoparticle-mediated methods discussed above, rather than modulating the signalling environment, it bypasses upstream signalling entirely by directly supplying the transcriptional machinery required for adipogenesis. The high biocompatibility and biodegradability of PLGA make this a particularly attractive platform for clinical translation.

In contrast to the pro-adipogenic materials discussed above, silica nanoparticles (SiNPs) were reported to exert a negative effect on adipogenic differentiation of hMSCs, as shown by Wang et al. **[69]**. SiNPs synthesised by the modified Stöber method (~50 nm) were readily internalised by hMSCs, as confirmed by TEM and confocal laser scanning microscopy. Exposure of hMSCs to SiNPs under adipogenic induction conditions resulted in a reduction in lipid droplet formation, decreased triglyceride content, and downregulation of adipogenic marker genes, in a size-dependent manner. The mechanistic basis was proposed to involve regulation of p38 MAPK phosphorylation, which alters the balance of adipogenic versus osteogenic transcription factor activity **[69]**. This stands in notable contrast to the behaviour of AgNPs and gold nanostructures discussed above, underscoring the central role of nanoparticle composition and surface chemistry in determining MSC differentiation outcomes, and cautioning against generalised assumptions about nanomaterial-cell interactions.

In summary, two broad mechanistic themes emerge. The first is ROS-mediated lineage modulation: AgNPs and MUA-AuNOs both elevate intracellular ROS, which at moderate, sustained levels activates the PPARγ transcriptional programme while suppressing RUNX2, thereby tipping MSC commitment towards adipogenesis over osteogenesis **[65, 66]**. The second is cytoskeletal and mechanotransduction-based lineage guidance: GO substrates and high-density RGD-AuNPs both act through surface chemistry and integrin clustering to promote a rounded, low-cytoskeletal-tension morphology that is permissive of adipogenic differentiation **[64, 67]**. The gene delivery approach of Kim et al. **[68]** represents a third, orthogonal mechanism, direct transcription factor delivery, that bypasses nanoparticle-cell surface interactions entirely. Together, these findings establish that nanomaterial-mediated control of MSC adipogenesis is achievable through diverse physical, chemical, and biological routes, with the specific outcome being highly dependent on nanoparticle composition, surface chemistry, geometry, and the presence or absence of chemical induction media.

Table 3: List of nanomaterials used for adipogenic differentiation and key adipogenic markers/observations

Nanomaterial	Particle Size (nm)	Stem Cell Type	Key Adipogenic Markers / Observations	Reference
Graphene oxide (GO) substrate	Sheet (lateral: variable)	hMSCs	Significantly greater lipid vacuole accumulation by Oil Red O staining vs. graphene and PDMS controls after 14 days under adipogenic induction. GO's hydrophilic surface facilitates adipogenic protein adsorption.	[64]
Silver nanoparticle (AgNP)-coated surfaces	~10–30 (deposited)	hBMSCs	Enhanced lipid droplet accumulation. PPARγ, ADD1, and C/EBPα upregulated. Mechanism: intracellular ROS accumulation → activation of antioxidant enzymes → enhanced adipogenic capacity.	[65]
MUA-functionalised gold nano-octahedra (MUA-AuNOs)	~50–80 (edge length)	bMSCs	Enhanced Oil Red O staining; PPARγ and FABP4 upregulated at mRNA and protein level. Osteogenic potential (ALP, ARS) concurrently weakened. ROS-mediated; structure- and dose-dependent.	[66]
RGD-modified gold nanoparticles (high ligand density)	~15–20	hMSCs	High RGD density promoted oil droplet formation and adipogenic marker gene expression via integrin clustering and reduced cytoskeletal tension. Low RGD density had inhibitory effect.	[67]
PEI-coupled PLGA nanospheres (C/EBPα + C/EBPβ delivery)	~200–400	hMSCs	Transfection efficiency: 28.96% (dual gene). Overexpression of C/EBPα and C/EBPβ significantly elevated adipogenesis confirmed by ORO, RT-PCR, Western blotting, and histology.	[68]
Silica nanoparticles (SiNPs)	~50	hMSCs	INHIBITORY effect. Reduced lipid droplet formation, decreased triglyceride content, downregulated adipogenic markers. Size-dependent; mechanism involves p38 MAPK phosphorylation regulation.	[69]

Chondrogenic Differentiation

Chondrocytes are the sole cellular constituent of cartilage, a tissue that lacks vasculature, innervation, and lymphatic supply, and consequently possesses an inherently limited regenerative capacity following injury or degeneration. Osteoarthritis, the most prevalent joint disease globally, is characterised by progressive cartilage degradation, and represents a major unmet clinical need for which MSC-based chondrogenic therapy offers considerable promise **[63]**. Chondrogenesis proceeds from a mesenchymal condensation event, in which MSCs undergo compaction and cell-cell contact, followed by commitment to the chondroprogenitor fate and terminal differentiation into mature chondrocytes embedded within a proteoglycan- and type II collagen-rich extracellular matrix **[70]**. The master transcription factor SOX9, together with its co-regulators SOX5 and SOX6 orchestrates the activation of chondrogenic target genes including type II collagen (COL2A1), aggrecan (ACAN), and cartilage oligomeric matrix protein (COMP) **[70]**. In vitro chondrogenesis is typically induced using transforming growth factor-β (TGF-β) isoforms (TGF-β1 or TGF-β3) and dexamethasone in pellet or aggregate culture, with confirmation by Alcian blue or toluidine blue staining for sulphated glycosaminoglycans (sGAG), immunostaining for type II collagen, and quantitative gene expression analysis of SOX9, COL2A1, and ACAN **[71]**.

Nanomaterials have been employed in chondrogenesis both as substrate materials that recapitulate cartilage-like ECM features and as non-viral gene delivery vectors for the direct transfer of chondrogenic transcription factors. A study by Park et al. **[71]** designed PLGA nanoparticles coated with polycistronic plasmid constructs encoding the SOX trio (SOX5, SOX6, and SOX9) for the chondrogenic induction of hMSCs. Dexamethasone-conjugated polyethyleneimine (DEX/PEI) was used as the transfection reagent to form dexamethasone-incorporated nanoparticles (DI-NPs). Compared to cells transfected with individual SOX genes, those receiving all three genes simultaneously via DI-NPs showed the highest upregulation of chondrogenic markers in microarray analysis. Specifically, SOX9, COL2A1, and ACAN were upregulated while the osteogenic marker collagen type I (COL1A1) was downregulated, indicating a selective chondrogenic commitment **[71]**. Chondrogenesis-induced hMSCs were further confirmed by RT-PCR, Western blotting, and immunohistochemistry. This gene delivery approach is mechanistically distinct from substrate-based methods: rather than providing biophysical cues, it directly supplies the transcriptional machinery required for chondrogenesis, drawing a parallel to the PEI-PLGA-mediated C/EBP delivery discussed in the adipogenic differentiation section.

Carballo-Pedrares et al. **[72]** explored cationic niosomes (non-ionic surfactant-based vesicles functionalised with a cationic lipid) as non-viral vectors for the delivery of SOX9 plasmid to primary bone marrow-derived hMSCs. Niosomes were synthesised via the thin-film hydration method and complexed with either conventional parental SOX9 plasmid or a minicircle SOX9 construct to form nioplexes. Physicochemical characterisation confirmed niosome diameters of approximately 150–200 nm and a positive zeta potential, ensuring electrostatic complexation with the negatively charged plasmid. hMSC aggregates were cultured for 21 days and evaluated by RT-PCR, immunohistochemistry, and histological staining. Cells transfected with the niosome–SOX9 complex showed significant upregulation of COL2A1, ACAN, and SOX9 itself over 21 days, confirmed by positive toluidine blue staining for proteoglycans and immunodetection of type II collagen. Importantly, the minicircle SOX9 construct outperformed the conventional parental plasmid in terms of chondrogenic gene expression and marker protein levels, attributed to its smaller size, higher transfection efficiency, and absence of bacterial backbone sequences that can trigger epigenetic silencing **[72]**. The absence of type X collagen (COL10A1) upregulation as an indicator of undesirable chondrocyte hypertrophy and endochondral ossification was a critical finding, establishing the suitability of this niosome-based approach for stable articular cartilage repair rather than transient fibrocartilage formation.

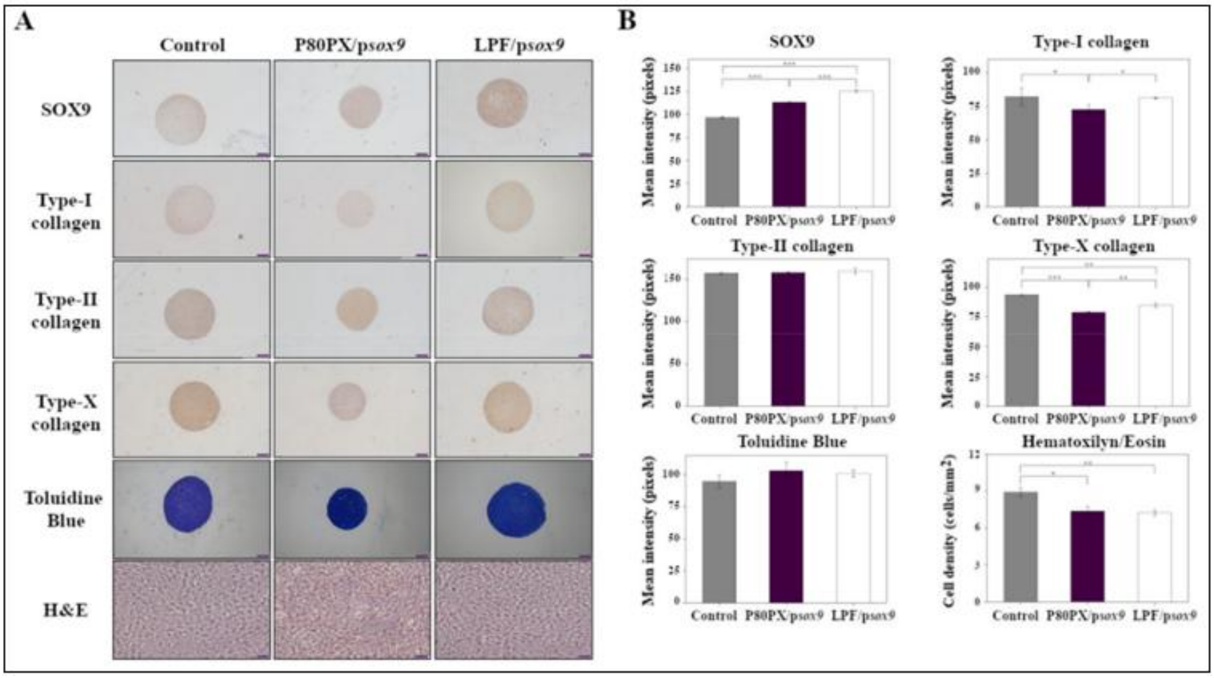

Figure 3: Immunohistochemical and histological analyses of hMSC aggregates cultured in chondrogenic medium (control; negative control) and transfected with psox9 via P80PX (P80PX/psox9) or LPF (LPF/psox9). Samples were kept in culture for 21 days and processed for (**A**) Immunodetection of SOX9, type-I, type-II and type-X collagen, and toluidine blue (all representative images; magnification 4X; scale bar 50 µm) or Hematoxylin/Eosin (H&E) stainings (all representative images; magnification 10x; scale bar 100 µm). (**B**) Histomorphometrical analyses (control: grey; P80PX/psox9: dark purple; LPF/psox9: white)* depicts $p < 0.05$, ** $p < 0.01$ and *** $p < 0.001$, when compared with denoted groups. Reproduced under CC BY 4.0 from [**72**].

In a substrate-oach, Xing et al. **[73]** examined the chondrogenic potential of polyelectrolyte multilayer (PEM) coatings incorporating collagen type I (Col I) and nano-hydroxyapatite (nHA) on tissue culture surfaces for human umbilical cord-derived MSCs (hUC-MSCs). The Col I/nHA surface consistently yielded the highest expression of SOX9, even in the absence of chemical chondrogenic inducers, while the expression of ACAN and COL2A1 was most prominently upregulated on Col I/nHA relative to all other PEM configurations tested under chondrogenic differentiation medium **[73]**. The mechanism proposed involves nHA providing a biomimetic ECM nanotopography that promotes MSC condensation and subsequent SOX9 activation, analogous to the mechanotransduction-driven differentiation described in the neurogenic and osteogenic sections. Alcian blue staining confirmed robust sGAG accumulation on Col I/nHA surfaces, and immunostaining for type II collagen was significantly positive in both basal and chondrogenic medium conditions, underscoring the capacity of the substrate nanotopography to partially substitute for chemical induction **[73]**.

A biologically distinct approach was demonstrated by Casanova et al. **[74]**, who developed an electrospun nanofibrous mesh (NFM) functionalised with anti-CD63 antibodies to immobilise extracellular vesicles (EVs) derived from human articular chondrocytes (hACs). EVs derived from hACs cultured in chondrogenic differentiation medium (NFM/EV-ACDM) were most effective at promoting chondrogenic commitment of hBM-MSCs under basal culture conditions over 28 days, inducing significantly higher expression of SOX9, COMP, ACAN, and COL2A1 compared to non-biofunctionalised NFMs cultured in chondrogenic medium ($p < 0.0001$) **[74]**. This result is particularly significant, as it demonstrates that EV-functionalised nanostructures can surpass the effect of soluble TGF-β-based chemical induction when EVs are of the appropriate biological origin and culture history. The NFM architecture serves as a structural scaffold that retains EVs at the cell-material interface, providing sustained paracrine signalling to the adherent MSCs and recapitulating the cartilage pericellular matrix niche more faithfully than suspension-based EV delivery **[74]**.

Across these studies, the primary markers used to confirm chondrogenic success are consistent: SOX9 as the early master regulator, COL2A1 and ACAN as mid-to-late matrix genes, sGAG accumulation by Alcian blue or toluidine blue staining, and the absence of type I collagen (COL1A1) and type X collagen (COL10A1) overexpression as evidence against fibroblastic or hypertrophic fates, respectively. The nanomaterials discussed span a mechanistic spectrum from direct transcription factor delivery (PLGA-SOX trio, niosomes-SOX9) to ECM-mimetic substrate nanotopography (Col I/nHA PEM coatings) to biologically active EV-functionalised nanostructures, collectively offering a diverse toolkit for cartilage tissue engineering applications.

Table 4: List of nanomaterials used for chondrogenic differentiation and key chondrogenic markers/observations.

Nanomaterial	Particle Size (nm)	Stem Cell Type	Key Chondrogenic Markers / Observations	Reference
PLGA NPs coated with polycistronic SOX5/6/9 plasmid (DI-NPs)	~200–400	hMSCs	SOX9, COL2A1, ACAN, and COMP upregulated; COL1A1 downregulated. Greatest effect with SOX trio co-delivery vs. individual SOX genes. Confirmed by microarray, RT-PCR, Western blotting, and immunohistochemistry.	[71]
Cationic niosomes (SOX9 delivery, minicircle plasmid)	~150–200	hBM-MSCs	Significant upregulation of COL2A1, ACAN, and SOX9 over 21 days. Positive toluidine blue and type II collagen immunostaining. No COL10A1 upregulation (no hypertrophic conversion). Minicircle > parental plasmid in efficiency.	[72]
Col I / nano-hydroxyapatite (nHA) polyelectrolyte multilayer coating	nHA: ~20–50	hUC-MSCs	Highest SOX9, ACAN, and COL2A1 expression across all PEM groups, including in basal medium. Alcian blue confirmed sGAG accumulation. Substrate nanotopography partially substituted for chemical induction.	[73]
Anti-CD63-functionalised electrospun NFM with immobilised chondrocyte-derived EVs	Nanofibre diameter: ~200–500; EVs: ~100–200	hBM-MSCs	SOX9, COMP, ACAN, and COL2A1 upregulation over 28 days under basal conditions surpassed standard TGF-β chemical induction ($p < 0.0001$). Sustained paracrine signalling via EV immobilisation.	[74]

Cardiomyogenic Differentiation

Myocardial infarction (MI) results in the irreversible loss of up to one billion cardiomyocytes, which the adult heart is functionally incapable of replacing, owing to the terminally post-mitotic nature of mature cardiomyocytes [**75**]. The resulting scar tissue impairs contractile function, predisposing the patient to arrhythmia, ventricular remodelling, and heart failure. The directed differentiation of MSCs into cardiomyocyte-like cells represents an attractive strategy for myocardial repair. However, MSC cardiomyogenic differentiation is inherently inefficient under conventional chemical induction protocols, which typically employ 5-azacytidine (5-Aza), a DNA demethylating agent that non-specifically activates cardiac gene loci [**75**]. The key transcription factors governing cardiac lineage commitment are Nkx2.5 and GATA4, which are activated early in cardiomyogenesis and drive the expression of the contractile protein genes α-myosin heavy chain (α-MHC), β-MHC, cardiac troponin T (cTnT), cardiac troponin I (cTnI), and α-sarcomeric actinin (α-SA). Gap junction protein connexin 43 (Cx43) is used as a functional marker of cardiomyocyte coupling [**75**, **76**]. The electrically conductive nature of the native myocardium has motivated particular interest in electroconductive nanomaterials, whose ability to propagate electrical signals between cells may provide critical biophysical cues that support cardiomyogenic differentiation.

Sun et al. [**76**] fabricated composite scaffolds of single-walled CNTs (SWCNTs, 0.7–1.2 nm diameter) non-covalently functionalised with collagen type I (CNT-Col) and examined their effect on brown adipose-derived stem cells (BASCs), which possess intrinsic cardiomyogenic potential. Compared to cells on pure collagen substrates, BASCs cultured on CNT-Col scaffolds showed significantly enhanced expression of the cardiac transcription factors Nkx2.5, GATA-4, and Tbx5 between days 3 and 10 of culture. The early markers α-MHC and β-MHC peaked at day 7, while cTnT followed a sustained upward trend throughout the culture period on CNT-Col, in contrast to the Col-only group. Mechanistic investigation revealed that CNTs activated the β1-integrin/TGF-β1 signalling axis in BASCs: blocking β1-integrin with a neutralising antibody abolished the cardiomyogenic enhancement, confirming that CNT-mediated integrin clustering and downstream TGF-β1 signalling were the primary drivers of the cardiomyogenic response [**76**]. This mechanistic finding distinguishes the CNT-mediated cardiomyogenic pathway from the ROS-driven and cytoskeletal tension mechanisms operative in adipogenesis and osteogenesis discussed previously.

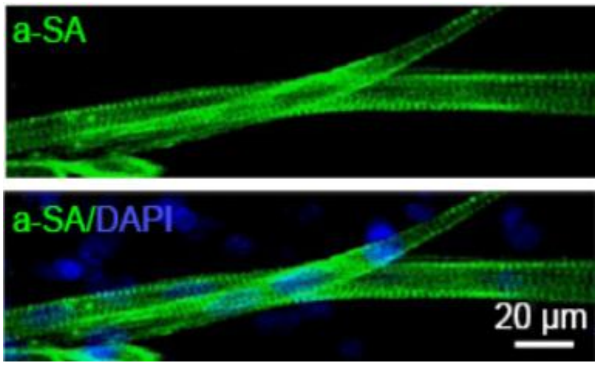

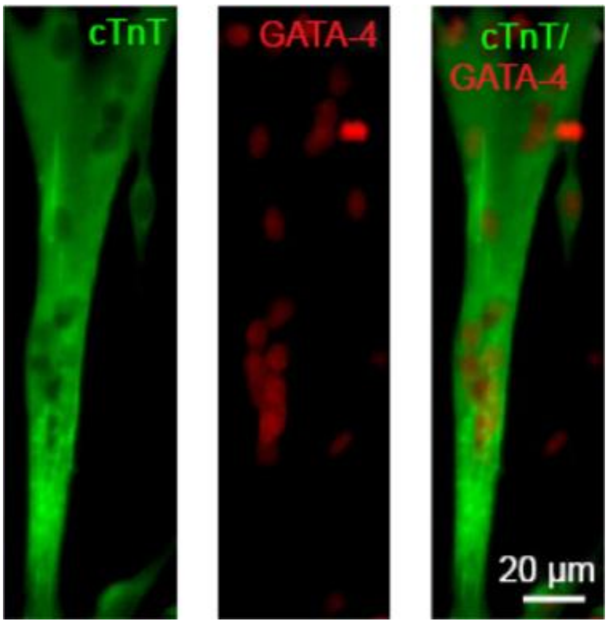

Figure 4: Immunofluorescence staining of cardiomyocyte-specific markers, including sarcomeric actin (a-SA, green) (B), double-stained for cTnT (green)/GATA-4 (red) and Nkx2.5 (green). Reproduced under CC BY 4.0 from [**76**]

The synergistic interaction between CNT-based scaffolds and chemical inducers was investigated by Wickham et al. [**77**], who electrospun composite scaffolds of poly(ε-caprolactone) with or without MWCNTs (PCL-CNT and PCL, respectively) to evaluate the cardiomyogenic differentiation of hMSCs. Under treatment with 5-Aza, Nkx2.5 and the late-stage cardiac markers α-MYH, cTNT, and ryanodine receptor 2 (RyR2) were all significantly upregulated on PCL-CNT substrates compared to PCL alone, confirming that the electrical conductivity of the carbon nanotube component synergised with the epigenetic action of 5-Aza to promote cardiomyogenic commitment [**77**]. Notably, extrinsic electrical stimulation on non-conductive PCL scaffolds without 5-Aza produced comparable cardiac gene upregulation, establishing that electrical signal propagation, whether delivered intrinsically by the conductive CNT network or applied extrinsically, is a key biophysical driver of cardiomyogenesis. This finding has important design implications: electroconductive CNT-based scaffolds may reduce the required concentration of toxic chemical inducers such as 5-Aza, improving the safety profile of cardiomyogenic differentiation protocols intended for clinical application.

Gold nanoparticle-functionalised scaffolds have also been explored for cardiomyogenic differentiation. Ravichandran et al. [**78**] fabricated electrospun PCL nanofibrous scaffolds loaded with AuNPs (~16 nm) and vitamin B12, and co-cultured hMSCs with cardiomyocytes on these composite mats. The AuNP-loaded scaffolds showed markedly higher cellular expression of CD44, α-actinin, and troponin compared to unloaded PCL controls, indicating enhanced cardiomyogenic commitment. The gold nanoparticles are proposed to improve electrical signal propagation between the co-cultured cells by providing conductive nanointerfaces at cell-material contact points, thereby mimicking the function of the native myocardial conduction system and promoting the synchronous contractile behaviour critical to cardiomyocyte maturation [**78**]. The addition of vitamin B12 further supports mitochondrial function and metabolic activity in the differentiating cardiomyocyte-like cells, providing a biochemical complement to the electrophysiological cues provided by the AuNPs.

The role of silver nanoparticles in cardiomyogenic differentiation was investigated by Mohammadi Amirabad et al. [**79**], who assessed the effect of AgNPs at 2.5 µg mL^{-1} on bone marrow-derived MSCs (BM-MSCs) with and without cardiomyogenic differentiation medium. In BM-MSCs cultured without differentiation medium (Group II), AgNPs alone enhanced expression of VEGF, von Willebrand factor (VWF), smooth muscle actin (SMA), and troponin T, indicating partial cardiomyogenic commitment in the absence of chemical inducers. In BM-MSCs cultured with differentiation medium (Group III), the addition of AgNPs significantly increased GATA4 protein and gene expression by approximately 1.20-fold and 1.27-fold, respectively, compared to differentiation medium alone. Mechanistic analysis revealed significant upregulation of Wnt-3 and β-catenin in both Groups II and III, implicating the Wnt/β-catenin signalling pathway as the operative mechanism [**79**]. Furthermore, AgNP treatment caused elongation of telomere length in treated BM-MSCs, which the authors proposed as a mechanism by which AgNPs maintain a transcriptionally active chromatin state conducive to differentiation. This telomere-based mechanism is mechanistically novel relative to the integrin/TGF-β1 and electrical conductivity pathways described for CNT- and AuNP-based systems, respectively.

Across these studies, a consistent biophysical theme emerges: the electrical conductivity of nanomaterial-based scaffolds, whether arising from carbon nanotube networks or gold nanoparticle interfaces, plays a uniquely important role in cardiomyogenic differentiation that is less prominent in other lineages. This reflects the electrophysiological nature of the target cell type, where calcium cycling, action potential propagation, and gap junctional coupling through Cx43 are intrinsic requirements for functional cardiomyocyte identity. Nanomaterials that restore or mimic these electrical microenvironmental cues therefore offer a mechanistically coherent approach to cardiomyogenic differentiation that conventional chemical induction with 5-Aza alone cannot provide. Silver nanoparticles represent an additional, chemically distinct mechanism of action, operating through Wnt/β-catenin signalling and telomere remodelling, and may prove complementary to conductive scaffold strategies in a combined-modality cardiomyogenic protocol.

Table 5: List of nanomaterials used for cardiomyogenic differentiation and key cardiomyogenic markers/observations.

Nanomaterial	Particle Size (nm)	Stem Cell Type	Key Cardiomyogenic Markers / Observations	Reference
SWCNT–collagen I composite scaffold (CNT-Col)	0.7–1.2 (diameter)	BASCs	Nkx2.5, GATA-4, and Tbx5 upregulated days 3–10. α-MHC and β-MHC peaked day 7; cTnT increased continuously. Mechanism: β1-integrin/TGF-β1 pathway activation. Blocking β1-integrin abolished the effect.	[76]
Electrospun PCL–MWCNT composite scaffolds (PCL-CNT)	MWCNT: ~10–30 (outer diameter)	hMSCs	Under 5-Aza treatment: Nkx2.5, α-MYH, cTNT, and RyR2 significantly upregulated on PCL-CNT vs. PCL alone. Conductive CNT network synergises with 5-Aza; electrical conductivity equivalent to extrinsic electrical stimulation.	[77]
AuNP-loaded PCL nanofibrous scaffolds (AuNP + Vit B12)	AuNPs: ~16	hMSCs (co-cultured with CMs)	Enhanced α-actinin, troponin, and CD44 expression. AuNPs improve intercellular electrical signal propagation at cell-material interfaces, mimicking native myocardial conduction.	[78]
Silver nanoparticles (AgNPs)	~20–50	BM-MSCs	Without induction medium: partial commitment (VEGF, VWF, SMA, troponin T). With induction medium: GATA4 protein ↑ 1.20×, gene ↑ 1.27×. Mechanism: Wnt-3/β-catenin signalling + telomere length extension.	[79]

Stem Cell Imaging

An important aspect of stem cell therapy is locating viable and transplantable MSCs, useful for differentiation using the abovementioned methods. For this, cellular imaging is employed. We observe the most efficient coupling of nanomaterials and biomolecules under specific conditions of temperature, pH, or salt concentration. Functionalisable NMs provide the opportunity for detection under various methods, which allow for distinct, non-invasive labelling. Stem cell labelling can be performed directly or indirectly. Direct labelling can be performed by directly adding small molecules to the cells during expansion in tissue culture. Such labels can be present on the cell surface or can be internalised. It is preferred to confine the labels to intracellular compartments to avoid background noise or dislodging of labels from the cell surface. Many different materials have been employed for the same. They can be categorized into soft materials and hard materials depending upon their composition.

Hard nanomaterials include inorganic nanocrystals with properties unique to their size. Magnetic nanomaterials, particularly superparamagnetic iron oxide nanoparticles (SPIONs), have been used extensively to track stem cells using MRI **[80]**. For cellular uptake, SPIONs are coated with biomolecules, such as dextran, to avoid deleterious effects **[81]**, improve stability and solubility **[82]**, and prevent aggregation **[83]**. Castaneda et al. described a protocol for enhancing signal intensity for MRI by using ferumoxytol and protamine to label human mesenchymal stem cells, human embryonic kidney 293 cells, and induced pluripotent stem cells, showcasing clear contrast on uptake within MR images **[84]**.

Quantum dots are nanomaterials where all three dimensions are in the nanoscale. Carbon-based quantum dots (CQDs) attract considerable attention due to their size, high photoluminescence quantum yield, improved surface grafting, and high water solubility **[85-89]**. They are highly resistant to photobleaching **[90]**. Zhu et al. synthesised CQDs with citric acid monohydrate and diethyl glycol BIS ether with high fluorescence, high biocompatibility, and a quantum yield of 11% **[90]**. Mukherjee et al. reported a green synthesis method of sulphur-doped CQDs using sugar molasses with a high fluorescence, biocompatible and a 47% quantum yield **[88]**. Another unique aspect of CQDs is their effect on stem cell differentiation, showcasing a high osteogenic potential while maintaining fluorescence **[88, 89]**. Such materials can be used for synergetic stem cell therapy.

Soft materials include lipid-based nanomaterials and polymeric nanomaterials. They are mainly used as encapsulation agents to deliver the label molecules. Hsieh et al. showed that liposome-mediated transfection effectively labeled hBMSCs with CdSe/ZnS QDs. Furthermore, the internalization of QDs did not significantly affect hBMSC proliferation but did inhibit osteogenic differentiation **[93,94]**. Polymeric NMs are used due to their high biocompatibility and low immune reactivity. Resmini et al. covalently linked fluorescent tags onto N-isopropyl acrylamide-based thermoresponsive nanogels RM1 and P(TEGA)-b-P($_{D,L}$LA)$_2$ nano-micelles RM2 and applied it in tracking neural stem cells from the postnatal subventricular zone without affecting its proliferation, multipotency and differentiation characteristics **[95]**. Wu et al. reported near-infrared fluorescent semiconductor polymer dots that possessed a narrow band emission at 775 nm and a quantum yield of 22% which could track stem cells for over two weeks when added with a penetrating peptide without disturbing their multipotency **[96]**.

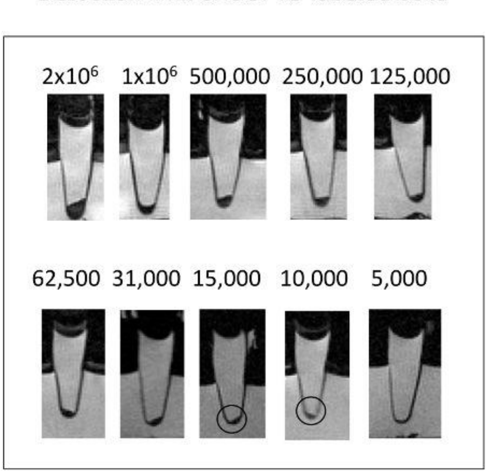

(a)

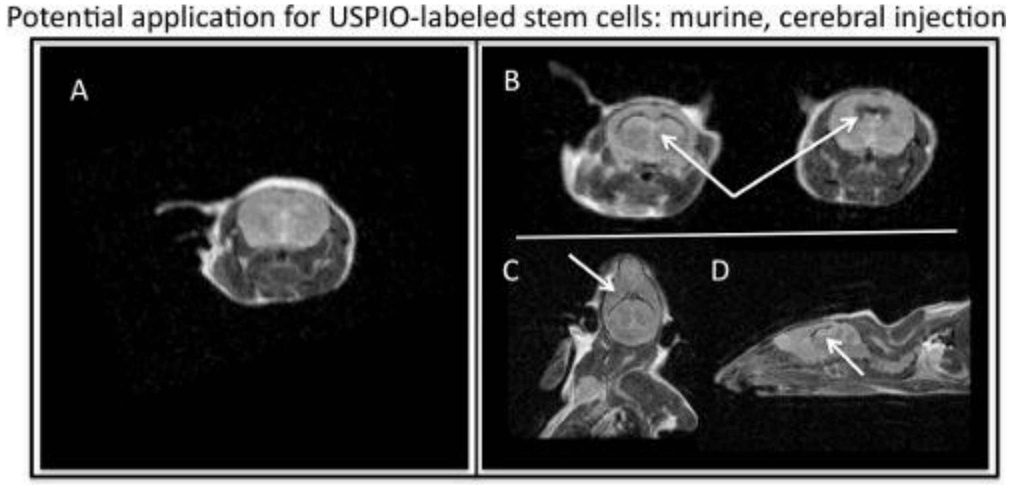

(b)

Figure 5: (a) Sagittal cross sections of Eppendorf tubes with cells in cell pellets. As little as 10,000 ferumoxytol-labeled cells can be detected via T2-w MR imaging. (b) MR visualization of ferumoxytol-labelled stem cells injected into the murine cerebral ventricle. Repurposed from [84] with permission

Indirect labelling introduces a reporter gene into the genome of the cell of interest to express receptors, enzymes, or fluorescent/bioluminescent proteins suitable for imaging cell location, number, function, and so forth **[92]**. Here, different soft and hard nanomaterials can be used as vectors for gene delivery. Negatively charged phosphate groups bind to the cationic polar head domain of a lipid-based NP and facilitate gene delivery. The linker group connects the polar domain to the hydrophobic domain of the NP and determines the chemical stability, biodegradability, and transfection efficiency of the lipid NPs **[93]**. To increase the efficiency of transfection, various formulations have been generated by tuning the head group size and hydrocarbon tail length **[94]**. The internalisation of lipoplexes – the complex formed between the polar head and the gene – occurs via endocytosis **[95]**. To avoid toxicity due to the cationic polar group, it is usually capped with polyethylene glycol, which improves circulation time by preventing reticuloendothelial system uptake **[96, 97]**.

Polymeric NMs carry the gene of interest via encapsulation and electrostatic interactions **[98]**. They are biocompatible, and biodegradable and yet degrade slowly to allow for effective gene delivery. To achieve both encapsulation and electrostatic interactions, polymers must contain cationic moieties. Poly(L-lysine) or PLL is a widely used polymer for gene delivery. However, it possesses some drawbacks, mainly due to unstable nucleic acid chains prone to enzymatic activity. To prevent this, PLL was copolymerized with HPG-C18 to form a star-shaped polymer for effective delivery of docetaxel and MMP-9 siRNA plasmid **[99]**. Biopolymers and NMs designed from biologically important molecules prove important for designing effective strategies for delivery and tagging stem cells for imaging.

Green synthesis methods for NMs involved in stem cell therapy (Mihir)

Ceramic NMs

Hydroxyapatite NPs (HAP-NPs) find their applications mainly in osteogenic differentiation, as discussed earlier. We have also discussed the application of HAP-NPs of various morphologies and their impact on osteogenic differentiation. Multiple different methods have been reported for its synthesis – including the combustion method **[100]**, hydrothermal method **[101]**, mechanochemical method **[102]**, electrochemical method **[103]**, sol-gel method **[104]**, and chemical precipitation **[105]**.

Wijesinghe et al. **[106]** reported a facile chemical precipitation method for needle-like and spherical HAP-NPs. They prepared a 0.05 M calcium sucrate solution (100.0 ml) by dissolving 2.80 g of CaO in 0.05 M sucrose solution. Then, 0.03 M ammonium dihydrogen orthophosphate (100.0 ml) was added drop-wise to the above calcium sucrate solution, to maintain the Ca/P mole ratio at 1.67. The mixture was then stirred for 24 hours. They studied six sets of products prepared at different temperatures, namely 10°C, 25°C, 40°C, 60°C, 80°C and 95°C, maintained for 2 hours. The precipitated product was then collected via centrifugation and washed with DI water three times. The products were dried for 12 hours in a vacuum oven. One product per set was then calcined at 700°C for 3 hours. On analysis, they observed that the X-ray diffraction patterns for the non-calcined samples showed sharper peaks with increasing preparation temperature. The SEM images showed a needle-like morphology for non-calcined samples that increased in average length and width with increasing preparation time. The average length increased from approximately 30.2 nm to around 130.4 nm, and the average width increased from around 10.4 nm to about 29.2 nm **[106]**. The calcined samples showed spherical morphology with an insignificant increase in average diameter (from around 89.6 nm to around 99.2 nm) with an increase in the preparation temperature **[106]**. The different morphologies can be attributed to the crystal growth under different conditions. The size of the nuclei depends upon the preparation temperatures **[106]**. Moreover, crystal growth occurs at a slower rate than nucleation. Thus, crystal growth on nuclei of different sizes shows different crystallite sizes. The activation energy for crystallization in the needle-like morphology is lower than that of the spherical morphology **[106]** and thus, the non-calcined samples showcase a needle-like morphology. Moreover, on calcination, the heat provided is sufficient to cross the activation energy barrier to allow crystal growth around the nuclei. The FTIR spectral analysis shows interesting peaks at

1458 cm^{-1}, 1422 cm^{-1} and 867 cm^{-1} corresponding to a carbonate group. However, the percentage of carbonation is as low as 0.8% which may suggest that some hydroxyl groups have been replaced with carbonate groups -sour**[106]**. This shows a similarity between HAP-NPs and bone apatite. This method provides a temperature-dependent control over morphological aspects of the synthesised nanoparticles.

Another study by Sherif Elbasuney **[107]** studied the hydrothermal synthesis of HAP NPs with various morphologies by mixing instantly two counter-current streams. To synthesise HAP nanoplates, 0.015 M dibasic ammonium phosphate was superheated at 300°C and 240 bar pressure. This superheated solution was passed down a nozzle pipe against an up flow of cold aqueous solution of 0.05 M calcium nitrate tetrahydrate, also at 240 bars. The flow of NPs was cooled and then collected. To synthesise nanorods, the pH of the aqueous solution was set to 10 using ammonium hydroxide. On TEM analysis, the size of the nanoplates was reported to be 400 nm in length and 150 nm in width **[107]**. However, the nanorods were 500 nm long and 10 nm in diameter **[107].** The size of the obtained nanoparticles may be larger than the ones previously studied, but this method provides a facile and scalable route for HAP NP synthesis.

A bio-sourced synthesis method reported by Vinayagram et al. **[108]** involves using Muntingia calabura leaf extract as a solvent and chicken eggshells as the calcium source. Eggshells were thoroughly cleaned once with tap water and then thrice with DI water. They were heated at 80°C for 30 minutes, desiccated at 80°C for 24 hours in a hot air oven, and then pulverized and annealed at 1000°C for 2 hours in a muffle furnace. This constitutes the CaO powder required for the synthesis. A stoichiometric amount of CaO solution was prepared in the leaf extract and stirred continuously on a hot plate for 2 hours. Orthophosphoric acid (molar ratio: 1.67 Ca/P) was added dropwise, stirred thoroughly for 30 minutes and then aged for 24 hours. The residue was centrifuged, rinsed with DI water, dried at 100°C for 2 hours and then calcined at 900°C for 2 hours. X-ray diffraction studies confirm a hexagonal phase for the HAP NPs synthesised. The average crystallite size was determined to be 30.39 nm by the Debye-Scherrer formula **[108]**. The SEM images show a rough and non-uniform surface morphology, which provides it with more surface area to increase cell adhesion, as also shown by Liu et al. **[109]**.

Gold Nanoparticles (AuNPs)

We have previously discussed the applications of gold nanoparticles within osteogenic differentiation. Gold nanoparticles have been historically used for various biological applications. The chemical preparation of colloidal AuNPs typically involves reducing Au salt in liquid with vigorous stirring, resulting in fairly uniform-sized nanoparticles, along with the addition of a reducing agent. Of various methods reported in the literature, multiple physical and chemical methods can be used to synthesise and control the size of AuNPs. For example, the Turkevich–Frens method yields monodisperse, water-soluble particles with a wide dimension range of 7-100 nm **[45, 46, 110]**. The Brust-Schiffrin method allows for synthesizing AuNPs with a diameter of 2 to 6 nm only **[47, 110]**. Moreover, chemical methods often produce toxic by-products. Thus, to mitigate this, various biological methods are being explored to synthesize AuNPs. These studies are based on the capping and reducing potential of various biological systems.

Various bacteria and yeast have been used to synthesize AuNPs. Mourato et al. **[111]** have reported producing AuNPs with diameters ranging from 30-100 nm. Yarrowia lipolytica NCIM 3589, a tropical marine yeast, synthesized 15 nm Au-NPs at pH 7.0 and 9.0 when incubated with $HAuCl_4$ solution **[112]**. This synthesis occurred via either constitutively produced NADH and NADH-dependent reductases or a protease enzyme, leading to the formation of NPs predominantly associated with and organized on the cell wall.

Moreover, various fungi are being used to synthesize AuNPs as well. Fungi have various advantages over other biological systems for synthesis: ease of handling and downstream processing, the ability to cover a large surface area **[113]**, and high tolerance towards metal ions **[114]**. Metal ions are converted into NPs by enzymes present in their cell walls and cytoplasm **[115]**. Moreover, it is also well known that filamentous fungi produce many secondary metabolites, namely polyketides, peptaibols, terpenes, pyrones, diketopiperazine, phenols, and alkaloids **[117-119]**. They also release extracellular proteins that stabilize the formed NPs **[116]**.

A recent study by Castro-Longoria et al. **[117]** showed the synthesis of AuNPs using the supernatant of Botrytis cinerea, Trichoderma atroviride, Trichoderma asperellum, Alternaria sp. and Ganoderma sessile. All strains were cultured in Erlenmeyer flasks containing 100 ml of PDB medium and placed in an incubator, where they were shaken at 120 rpm until approximately 10g of biomass was obtained. The biomass was washed with sterile deionized water, then incubated with shaking at 120 rpm for 72 hours at 30°C. After that, the supernatant was obtained by filtration, placed in 50 ml Falcon tubes, and centrifuged at 10,000 rpm for 10 minutes at 22°C. The supernatant was decanted and filtered with a vacuum pump using a 0.45 μm nitrocellulose membrane, then filtered again with a 0.22 μm nitrocellulose membrane (MF-Millipore) using a 25 mm filter in a 20 ml syringe. Finally, the supernatant of each strain was stored in a sterile flask at room temperature in the dark until used for the synthesis. The supernatant of each fungus was mixed with $HAuCl_4$ solution in a 1:3 v/v ratio. The pH was adjusted to 10 using 0.5 mM NaOH solution. UV-visible spectroscopy confirmed the formation of AuNPs with various absorption peaks, attributed to the different surface plasmon resonance. The peaks ranged from 525 and 550 nm, which indicate the formation of small, spherical NPs ranging from 9-20 nm **[117]**.

Plant extracts from different plant parts are used to synthesize AuNPs, as they are environmentally friendly sources rich in organic compounds that serve as reducing and stabilizing agents. Reactive compounds include flavonoids, amino acids, carboxylic acids, ketones, phenols, and proteins. Using plant extracts does not require aseptic environments **[120]**. Salix alba or white willow tree leaves have been collected by Ul Islam et al. **[121]** for the synthesis of AuNPs. At different pH, temperature, and concentration of NaCl, $HAuCl_4$ was reduced to stable AuNPs. The average particle size was reported to be 50-80 nm, stabilised at acidic pH and temperatures around

80°C **[121]**. Moreover, various organic molecules are responsible for various sizes and morphologies. Artocarpus hirsutus leaves possess polyphenols, flavonoids, and terpenoids which help in the synthesis of spherical nanoparticles with an average particle size of 5-40 nm within 6 hours **[122]**. Berries and citrus fruits are also known to synthesise AuNPs because they are rich in antioxidants **[123]**. Citrus maxima fruit extract creates spherical NPs with an average size of 15-35 nm **[124]**. Pear extracts are known for synthesising NPs with various morphologies: triangular, hexagonal, and polyhedral with an average size of 20-400 nm **[125]**.

Selenium Nanoparticles (SeNPs)

Selenium nanoparticles are special kinds of nanomaterials due to the various activities they perform within a biological system. Selenium is a part of proteins containing amino acids like selenomethionine, selenocysteine, and methylselenoysteinine **[126, 127]** and is needed for proper muscle function **[128]**. Moreover, selenium nanoparticles are known to possess low toxicity and antimicrobial and anticancer activities **[129-131]**. We have also explored the usage of SeNPs within osteogenic differentiation **[50]**.

There have been multiple methods reported for the synthesis of SeNPs, namely laser ablation **[132, 133]**, chemical synthesis **[134, 135]** and biosynthesis **[136, 137]**. Shoueir et al. **[135]** reported an eco-friendly microwave technique by carrying out the reduction of Na_2SeO_3 with ascorbic acid with the aid of polyvinyl alcohol (PVA) as a capping and stabilizing agent. After adding, the solution was collected in a Teflon-lined microwave reactor at 800W. The orange solution was centrifuged and the NPs were obtained. The NPs were washed twice with deionized water (DDI) and then twice with absolute ethanol for purification. The sample was dried in an oven at 50°C overnight to obtain a fine black powder. UV-Vis spectral analysis confirms the formation of SeNPs, owing to the peak observed at 297 nm due to their SPR lying between 200 to 400 nm **[138]**. X-ray diffraction studies also confirm the formation of high-purity SeNPs with a crystallite size of ~37 nm **[135]**. TEM analysis showcases a semi-spherical morphology with sizes ranging from 8.5-22 nm **[135]**.

Shar et al. **[136]** reported a green, hydrothermal method which involves the reduction of 10 mmol sodium selenite Na_2SeO_3 dissolved in 200 mL deionized water (DI water). To this solution, 4 g of L-ascorbic acid dissolved in 20 ml of DI water was added dropwise for 10 mins. The colour change to a dark colour indicated the formation of SeNPs. The product was centrifuged for 10 mins at 8000 rpm, rinsed with DI water, and then vacuum dried at 60°C. UV-Vis spectral analysis showed two peaks at 212 nm, indicating the smaller size of the NPs, and 274 nm, indicating aggregation of NPs **[136, 137, 139-141]**. X-ray diffraction studies confirm the formation of hexagonal NPs, also corroborated with the TEM analysis. The mean particulate size was observed to be 169.11 nm **[136].** This is higher than the previous study **[135]** which also showcased a similar synthesis mechanism.

Biosynthesis of SeNPs is a simple, one-step process without using toxic chemicals, high temperatures, or complex equipment. Biosynthesis can be achieved directly in living organisms or through bioreagents extracted from living organisms. Such nanoparticles are reported to possess lower toxicity, biodegradability and biocompatibility **[142]**. The reported mechanism involves using a precursor, like sodium selenite, sodium selenate, selenous acid or selenium dioxide, and placing it in a bacterial or fungal culture, plant extract, etc **[143-145]**. After this, Se ions' reduction confirms the presence of colloidal SeNPs, which are then stabilised and capped **[142, 146]**. Thus, multiple reports in recent years have revealed various strategies for the synthesis of SeNPs.

Cittrarasu et al. **[147]** have showcased the synthesis of SeNPs mediated by Ceropegia bulbosa Roxb extract. The nanoparticles were substantiated preliminarily via UV-Vis spectrum peak at 277.5 nm due to their SPR. X-ray diffraction studies confirmed the presence of SeNP nanoparticles. The average particle size was reported to be 55.9 nm. Another study by Puri et al. **[148]** used Tinospora cordifolia stem extract for SeNP synthesis. Here, the stem extract was added dropwise to 300 mM selenous acid with constant stirring. 2 mL of 400 mM ascorbic acid was then added to initiate the reduction reaction. The mixture was incubated for 24 hours and then centrifuged. The pellet obtained was rinsed and dried, suspended in PBS, ultrasonicated, centrifuged and dried again. UV-Vis spectral analysis confirms the formation of SeNPs by the peak obtained at 285 nm **[148]**, close to the peak obtained by Cittrarasu et al. **[147].** The XRD patterns do not show any sharp peaks, indicating that the particles obtained were amorphous. The Debye-Scherrer equation determined a crystallite size of 85 nm **[148]**. The average particle size was found to be 168.31 nm **[148]**.

Akçay et al. **[149]** reported the synthesis of SeNPs using Bacillus sp. EKT1 strain, cultured on a sterilized agar medium enriched with 1.9 mM SeO_2 at 33 °C for 24 h. Stocks were maintained in nutrient broth containing 50% glycerol (v/v) at -65 °C. To produce the NPs, the strains were transferred to a nutrient agar plate using a sterile loop. After being incubated at 33°C for 24 hours, a single colony was transferred to a sterile Erlenmeyer flask containing 30 mL of nutrient broth. The culture was then incubated on a shaking incubator for 24 hours at 33°C and 120 rpm. The seed culture was adjusted to an optical density of 2.0 and used to inoculate a sterile Erlenmeyer flask containing nutrient broth at 5% (v/v). After being incubated on a shaking incubator at 33°C for 24 hours, the supernatant was clarified using a refrigerated centrifuge (Hettich Universal, 320 R, Tuttlinger, Germany) at 4°C, 13,130 x g for 20 minutes. The clarified supernatant was then transferred into a final sterile Erlenmeyer flask for SeNP synthesis. SeO_2 solution is then added to this flask and reacted on a shaking incubator at 33 °C and 120 rpm for 72 h. FESEM images confirm that spherical particles were obtained with a mean diameter of 126 nm. Moreover, 68% of the particles obtained lie in the 50-150 nm range, which is acceptable in the nanoscale. The synthesis of SeNPs via this method is attributed to extracellular enzymes **[149]**.

ZnO Nanoparticles

ZnO nanoparticles show a large electrochemical coupling coefficient, high photostability, biocompatibility and low toxicity. Along with showcasing a strong UV absorption and high room-temperature exciton binding energy, on the biological front, ZnO showcases strong antibacterial activity and osteogenic differentiation potential **[51, 150-153]**.

Various physical, chemical, biological and hybrid processes for ZnO NP synthesis have been reported. Physical methods involve laser ablation **[154]**, physical vapour deposition **[155]** and more. Chemical methods involve sol-gel **[156]**, hydrothermal **[157]**, microwave irradiation, pyrolysis, chemical precipitation, microemulsion **[158]**, thermal decomposition of precursors, etc **[150]**. The biosynthesis method uses microorganisms or extracts of plants along with a precursor to form the nanoparticles.

Sol-gel method is considered to be one of the most advantageous and inexpensive methods due to its ease, high reproducibility and consistency. In line with that, a study by Iqbal et al. **[159]** reports a sol-gel method of synthesis by using zinc nitrate as the precursor. Briefly, 0.1 M $Zn(NO_3)_2.6H_2O$ was heated to 60°C. NH_4OH was added to adjust the pH to 8.5. The dispersed particles in the solution were obtained by centrifugation and then the precipitate was filtered and dried. UV-Vis spectral analysis confirms the formation of ZnO NPs with the observed absorbance at 300 nm owing to its SPR.

The biosynthesis of ZnO NPs has been extensively studied due to its low costs and energy expenditure, simpler synthesis procedure, and high synthesis rate **[160]**. Plant extracts contain various phytochemicals – flavonoids, tannins, alkaloids, amino acids, and proteins **[150]**. These compounds possess the ability to reduce metal ions into nanoparticles. Moreover, the polyphenols can chelate metal ions to form coordinated complexes, which are thermally decomposed to obtain the target nanoparticles. In line with that, Aldeen et al. **[150]** synthesized ZnO nanoparticles using Phoenix roebelenii extract by dissolving $Zn(NO_3)_2.6H_2O$ in 100 mL of the extract for ~20 hours. The obtained precipitate was collected via centrifugation, washed, dried and calcined at 500°C for 2 hours. X-ray diffraction studies confirm a hexagonal wurtzite structure (P63mc). The average crystallite size was found to be 11.4 nm **[150]**. The TEM images confirm the particle size to be in the range of 8-25 nm.

Another study by Pham et al. **[161]** describes ZnO NP synthesis using orange fruit peel extract. Zinc nitrate was added to the peel extract and stirred for 60 minutes and then placed in a water bath at 60°C for 60 minutes. Then, the mixtures were dried at 150°C and then heat-treated at 400°C for 1 hour. TEM image analysis showcased spherical particles with sizes between 10-20 nm. X-ray diffraction analysis confirms a hexagonal wurtzite structure. We observe in both the abovementioned studies that small particle sizes are obtained. Moreover, the wurtzite structure is the most thermodynamically stable, which is achieved by using plant extracts.

More interestingly, the same study by Iqbal et al. **[159]** compared their sol-gel method with a green synthesis method using various plant extracts. The UV-Vis spectral analysis confirmed the formation of ZnO NPs. Moreover, EDX analysis showcases an optical absorption peak at 1 keV, confirming the presence of Zn **[162]**.

Carbon Nanotubes

Carbon nanotubes (CNTs) are 1D carbon nanomaterials consisting of graphene sheets rolled into seamless hollow cylinders. Depending on the number of concentric graphene walls, they are classified as single-walled carbon nanotubes (SWCNTs), with diameters of 1–2 nm, or multi-walled carbon nanotubes (MWCNTs), with outer diameters ranging from 2 to 100 nm and lengths extending to several hundred microns [**163**]. Their extended aromatic C–C bond network imparts exceptional mechanical strength, high electrical conductivity, and a large surface area, which, as discussed in the neurogenic differentiation section, underpins their utility as substrates for directed stem cell behaviour [**21**, **22**].

Conventional synthesis of CNTs, primarily through arc discharge, laser ablation, and chemical vapour deposition (CVD), typically requires high temperatures, metal catalysts such as Fe, Co, or Ni, and complex vacuum equipment, generating toxic by-products and metal-contaminated products [**163**, **164**]. To mitigate these concerns, biomass-derived and plant-mediated approaches to CNT synthesis have been extensively explored. These green methods leverage naturally occurring carbon-rich molecules as precursors, reducing agents, and in some cases, as catalysts, thereby eliminating or significantly reducing the use of hazardous chemical inputs.

A widely reported green carbon source for CNT synthesis is camphor ($C_{10}H_{16}O$), a crystalline lactone extracted from the Cinnamomum camphora tree, which is widely distributed across sub-tropical regions including India, China, Japan, and Indonesia. Thermal decomposition of camphor at 875 °C under an inert argon atmosphere produces a heterogeneous mixture of aligned CNTs, alongside MWCNTs and SWCNTs [**165**]. The high hydrogen content and rigid bicyclic structure of camphor facilitate efficient carbon ring formation during pyrolysis, enabling the nucleation and growth of tubular graphitic structures. The resulting vertically aligned CNTs (VACNTs) are geometrically constrained relative to their randomly oriented counterparts, providing a well-defined surface nanotopography which, as reported by Tay et al. [**21**], is directly relevant to stem cell differentiation outcomes.

Islam et al. [**166**] demonstrated an unconventional concept of using plant extracts directly as the catalyst source for CVD growth of MWCNTs, dispensing with the conventional metal catalyst entirely. In their approach, extracts of several plant species, including walnut and other botanicals, were used as the catalyst precursor in a simple CVD system operating at as low as 575 °C, a notably lower growth temperature than any previously reported metal-catalysed CVD process. The use of walnut extract at 800 °C further yielded SWCNTs alongside carbon nano-belts with a hollow rectangular cross-section. Characterisation via transmission electron microscopy (TEM) and Raman spectroscopy confirmed the graphitic nature of the product, with the characteristic D band (~1350 cm^{-1}) and G band (~1580 cm^{-1}) clearly resolved in the spectra. The key advantages of this approach are threefold: the grown CNTs are entirely free of residual metal catalyst contamination, growth temperatures are significantly lower than those used conventionally, and the synthesis requires no expensive vacuum infrastructure [**166**].

A wholly catalyst-free approach to MWCNT synthesis was demonstrated by Duraia et al. [**167**], who performed thermal annealing of yellow corn seeds under a hydrogen atmosphere without any external catalyst or complex processing. The one-step green approach capitalises on the high carbon content and porous microstructure of corn seeds, which serve simultaneously as the carbon source and the structural template for nanotube nucleation. Raman spectroscopy confirmed the successful formation of MWCNTs, evidenced by the D band at approximately 1350 cm^{-1} and the G band at approximately 1580 cm^{-1}, with the G band intensity indicative of a high degree of sp^2 graphitisation. This method is particularly notable for its simplicity- bypassing the need for catalyst preparation, controlled gas-phase delivery systems, or post-synthesis acid washing steps conventionally required to remove metal impurities.

A complementary functionalization strategy was reported by Alhajri et al. [**168**], who produced silver-functionalised MWCNTs (SFMWCNTs) using an olive leaf extract. Olive leaf extract is rich in oleuropein, hydroxytyrosol, and related polyphenolic compounds, which act as reducing and stabilising agents for silver ions, driving their deposition onto the nanotube surface. The resulting SFMWCNTs were characterised by UV-Vis spectroscopy, where a characteristic plasmon resonance peak confirmed the successful anchoring of Ag nanoparticles, and by FTIR spectroscopy, which revealed the retention of polyphenolic capping groups on the nanotube surface. This approach is significant for the field of stem cell therapy, as it combines the nanotopographic cues of MWCNTs with the biochemical signalling of silver nanoparticles, offering a multifunctional platform. Moreover, the absence of toxic by-products inherent to green synthesis improves the biocompatibility profile of the resulting composite [**168**].

Across these green CNT synthesis methods, a consistent mechanistic picture emerges. Biomass-derived carbon precursors undergo thermal decomposition, generating reactive carbon species, primarily acetylene (C_2H_2) and other hydrocarbons, that dissolve into the catalyst or template surface and subsequently precipitate as ordered graphitic sheets upon supersaturation, wrapping around nucleation sites to form tubular structures [**164, 165**]. In catalyst-free approaches, the microstructural pores and mineral phases of the biomass feedstock serve as substitute nucleation templates. The tunability of this process, achieved by varying pyrolysis temperature, atmosphere composition, and feedstock chemistry, offers a degree of control over the diameter distribution and wall number of the resulting CNTs, parameters which have direct implications for the mechanical and electrochemical properties relevant to stem cell substrate design.

Graphene NMs

Graphene is a single-atom-thick sheet of sp^2-hybridised carbon atoms arranged in a honeycomb lattice, exhibiting exceptional electrical conductivity, mechanical stiffness, optical transparency, and a high theoretical surface area of approximately 2630 $m^2\ g^{-1}$ [**169**]. Graphene oxide (GO) and reduced graphene oxide (rGO) have been the focus of this review. The presence of oxygen-containing functional groups on GO (epoxy, hydroxyl, and carboxyl groups) confers hydrophilicity and surface reactivity, while their partial removal in rGO restores electrical conductivity. Both properties are exploited in the design of neurogenic substrates [**23**].

Conventional chemical reduction of GO to rGO employs reagents such as hydrazine hydrate (N_2H_4) or sodium borohydride ($NaBH_4$), which, despite their high reduction efficiency, are acutely toxic, volatile, and pose significant environmental and occupational hazards [**170**]. Plant-extract-mediated reduction of GO provides a compelling green alternative, as the polyphenolic compounds, flavonoids, terpenoids, and organic acids abundant in plant extracts serve simultaneously as reducing and capping agents, with no requirement for stabilisers to prevent rGO aggregation [**170, 171**]. The majority of these strategies begin with GO prepared by Hummer's method or its modifications, followed by green reduction in a separate step.

Suryawanshi et al. [**171**] prepared rGO using an aqueous extract of Mangifera indica L. (mango) leaves and Solanum tuberosum L. (potato) as the reducing agents. A GO suspension prepared by Hummer's method was mixed with the respective phytoextract and the reduction was carried out at 60–70 °C. X-ray diffraction (XRD) analysis of the parent GO showed a characteristic (002) diffraction peak at $2\theta = 10.36°$ with a d-spacing of 0.85 nm, significantly larger than the 0.335 nm d-spacing of pristine graphite, reflecting the intercalation of oxygen-containing functional groups. Upon reduction, this peak broadened and shifted to a higher angle of approximately 23–26°, consistent with the partial restoration of the graphitic stacking order and the removal of oxygen moieties. Raman spectroscopy further confirmed the reduction, showing an increase in the D to G band intensity ratio (I_2/I^G) from GO to rGO, indicative of an increased density of sp^2 domains formed during deoxygenation. FESEM and TEM images revealed the characteristic crumpled sheet morphology of rGO, while zeta potential measurements confirmed colloidal stability in aqueous suspension [**171**].

A study by Kumar et al. [**172**] reported the green reduction of GO using an extract of Tagetes erecta (marigold) flowers, chosen for their high content of lutein, quercetin, and other flavonoid antioxidants capable of donating electrons to reduce the epoxide and hydroxyl groups on the GO surface. GO was prepared by Hummer's method, and the dried flower extract was dissolved in deionised water and added dropwise to the GO dispersion under continuous stirring. The colour change of the mixture from brown to black was used as a preliminary indicator of reduction. XRD analysis confirmed the disappearance of the GO peak at ∼10° and the emergence of a broad peak around 25°. FTIR spectroscopy demonstrated a significant reduction in the intensity of hydroxyl (–OH, 3400 cm^{-1}), epoxide (C–O–C, 1230 cm^{-1}), and carbonyl (C=O, 1720 cm^{-1}) stretching bands, directly evidencing the removal of oxygen-bearing functional groups [**172**]. TEM images revealed a layered sheet structure consistent with few-layer rGO. The resulting rGO was probed for diverse biomedical applications, underscoring the growing interest in biocompatible, plant-reduced graphene materials.

Pandiyan et al. [**173**] explored a similar strategy using aqueous polyphenol extracts of Dendrobium anosmum orchid flowers as the reductant. UV-Vis spectroscopy of the parent GO showed an absorption peak at approximately 229 nm corresponding to the π–π* transitions of C=C bonds, with a shoulder at ~300 nm attributed to n–π* transitions of carbonyl groups. After green reduction, this peak red-shifted to 270–274 nm, confirming the recovery of the conjugated π electron system of graphene. Raman spectral analysis showed the D band at 1338 cm^{-1} and the G band at 1568 cm^{-1}. The I_2/I^G ratio for the green-reduced product (1.04) was higher than that of GO (0.89), reflecting the creation of new sp^2 domains upon reduction, consistent with findings from other plant-mediated rGO studies [**173**]. SEM images revealed a crumpled, coregulated surface morphology in GO transitioning to a more expanded, high-surface-area architecture in the reduced product. This structural evolution is directly relevant to stem cell applications, as a higher accessible surface area facilitates the adsorption of serum proteins and growth factors that direct cellular fate decisions.

Importantly, Tinospora cordifolia was used by Puri et al. **[148]** for SeNP synthesis, and also by researchers for the green reduction of GO to rGO [**174**], underscoring the versatility of a single biological extract across multiple nanomaterial systems. In the latter study, the T. cordifolia extract was mixed with a GO suspension under mild heating, and HD-XRD confirmed increased crystallinity in the green-rGO product. FTIR confirmed improved oxygen functional group removal, and the material showed a hydrodynamic radius of 270–470 nm with an average zeta potential of −29.9 mV, confirming stable colloidal dispersion [**174**]. These properties are particularly relevant for the synthesis of the GO-Au nanocomposite reported by Hung et al. [**23**], where the surface chemistry of the GO component directly governs the efficiency of gold nanoparticle deposition and the subsequent neurogenic differentiation response.

The mechanistic basis of plant-mediated GO reduction lies in the electron-donating capacity of polyphenolic and flavonoid compounds, which reduce the epoxide and hydroxyl groups on the basal plane and edge of the GO sheet via oxidation of their own hydroxyl moieties [**176**]. The long-chain organic molecules in the extract simultaneously adsorb onto the rGO surface, preventing re-aggregation and providing a residual capping layer. This dual role, as both reducing and stabilising agent, distinguishes plant-extract-mediated synthesis from conventional chemical reduction, where a separate stabiliser such as polyethylene glycol or sodium dodecyl sulphate is typically required. The degree of reduction measured by the I_2/I^G ratio and by the FTIR reduction efficiency is influenced by the composition of the extract, the GO-to-extract ratio, the temperature, and the reaction time [**176**]. Optimising these parameters is therefore an active area of research, as a higher reduction efficiency translates directly to better-restored electrical conductivity, which, as discussed in the neurogenic differentiation section, is a key driver of the neurogenic response in MSCs cultured on rGO-based substrates [**173**].

3. Conclusion

This review has examined the rapidly expanding role of nanomaterials in two principal domains of stem cell therapy: the directed differentiation of mesenchymal stem cells towards therapeutically relevant lineages, and the non-invasive imaging and tracking of transplanted stem cell populations. Across both domains, the physicochemical properties of nanomaterials, including their composition, size, morphology, surface chemistry, and mechanical and electrical characteristics, are active determinants of stem cell behaviour, operating through a diverse and lineage-specific set of biological mechanisms.

In the context of directed differentiation, five distinct lineages have been considered. Neurogenic differentiation is driven predominantly by nanotopographical cues: carboxylated SWCNT films, PDMS nanogratings, and three-dimensional nanostructured microarchitectures all exploit mechanotransduction to upregulate MAP2, GFAP, nestin, and β-tubulin without chemical induction, while GO–Au nanocomposites engage the SDF-1/CXCR4 chemokine axis to produce the most pronounced fold-changes in neurogenic markers yet reported for a nanomaterial system.

Osteogenic differentiation operates through the broadest mechanistic repertoire of any lineage reviewed: HAP-based composites and AuNPs act through p38 MAPK and ERK signalling to activate RUNX2 and BMP-2; SeNPs and C-ZnO nanofibers drive early mineralisation via ALP and osterix upregulation; and a distinct immunomodulatory sub-programme, activated by hydrophilic Ti surfaces, anionic polymer coatings, Cu-doped bioceramics, and GO–CaP nanomaterials, controls osteogenesis indirectly by polarising macrophages toward the M2 anti-inflammatory phenotype and suppressing foreign body giant cell formation. Together, these findings establish immunomodulation as a mechanistically independent, and clinically underexploited, route to nanomaterial-directed osteogenesis.

In the adipogenic lineage, two overarching mechanisms are apparent. First, ROS-mediated lineage modulation, operative in both AgNP-coated surfaces and MUA-functionalised gold nano-octahedra, activates the PPARγ/C/EBPα transcriptional programme while suppressing RUNX2, illustrating the reciprocal nature of the osteogenic–adipogenic fate balance and the sensitivity of that balance to nanomaterial-induced oxidative signalling. Second, integrin clustering and cytoskeletal tension modulation, exemplified by RGD-density-tunable AuNPs and GO substrates, provide a biophysical route to adipogenic commitment that is entirely independent of chemical inducers. The inhibitory effect of silica nanoparticles on adipogenesis via p38 MAPK regulation serves as an important counterpoint, reinforcing that the direction of nanomaterial influence on MSC fate is not universal but is acutely sensitive to compositional and surface chemistry differences between materials.

Chondrogenesis and cardiomyogenesis present the clearest cases for nanomaterial-mediated gene delivery as a differentiation strategy. In the chondrogenic lineage, PLGA nanoparticles and cationic niosomes each delivered SOX transcription factors with high fidelity, inducing robust COL2A1, ACAN, and proteoglycan expression while avoiding the hypertrophic conversion, marked by COL10A1 upregulation, that undermines conventional TGF-β induction protocols for articular cartilage repair. The EV-functionalised electrospun nanofibrous mesh is particularly noteworthy in this context, as it demonstrates that nanostructures can serve not only as static scaffolds or direct signalling agents, but as dynamic retention platforms for biological effectors, surpassing the gold standard TGF-β induction in chondrogenic output. In the cardiomyogenic lineage, the electrical conductivity of CNT-composite and AuNP-decorated scaffolds emerges as the defining biophysical requirement, directly reflecting the electrophysiological identity of the target cell type. The finding that CNT network conductivity can substitute for extrinsic electrical stimulation and reduce dependence on the genotoxic agent 5-azacytidine has immediate practical implications for the clinical safety of cardiomyogenic differentiation protocols.

In the domain of stem cell imaging, the complementary strengths of hard and soft nanomaterials have been demonstrated across multiple modalities. Superparamagnetic iron oxide nanoparticles, particularly ferumoxytol-based formulations, provide sensitive MRI tracking at cell numbers as low as 10,000 labelled cells, while dextran and other biocompatible coatings mitigate their immunogenic and aggregative liabilities. Carbon quantum dots occupy a uniquely advantageous position within the imaging landscape, combining high photoluminescence quantum yield, resistance to photobleaching, and demonstrated osteogenic differentiation potential in a single material platform. This property positions them as a theranostic agent capable of simultaneously reporting on and influencing stem cell fate. Polymeric nanomaterials, including thermoresponsive nanogels and near-infrared fluorescent semiconductor polymer dots, extend stem cell tracking beyond two weeks without compromising multipotency.

The green synthesis section of this review highlights the sustainability and translatability of potential synthesis routes. Across the five nanomaterial classes reviewed: hydroxyapatite, gold nanoparticles, selenium nanoparticles, zinc oxide, and carbon nanomaterials, plant-extract-mediated, fungal, and biosynthetic routes consistently yield nanoparticles of comparable or superior biological performance to those produced by conventional chemical methods, while eliminating toxic reducing agents, metal catalyst contamination, and high-energy processing requirements. Materials synthesised without cytotoxic by-products present a meaningfully reduced biocompatibility burden when translated to in vivo and eventually clinical settings.

Notwithstanding these advances, several challenges must be addressed before nanomaterial-directed stem cell therapy reaches widespread clinical application. First, the vast majority of studies reviewed here were conducted in two-dimensional in vitro culture systems, and the performance of many of these nanomaterials in three-dimensional tissue constructs, organoids, or in vivo models remains incompletely characterised. Second, the long-term fate of internalised nanomaterials, namely their biodistribution, clearance, and potential for accumulation in non-target organs, requires systematic investigation for each material class, particularly for metallic nanoparticles and carbon nanomaterials, whose biodegradability profiles differ substantially from those of polymeric and ceramic systems. Third, the dose-dependency and window of therapeutic action are critical parameters that are inconsistently reported across the literature; the inhibitory effect of SiNPs on adipogenesis and the cytotoxic threshold of AgNPs serve as reminders that the beneficial and deleterious effects of nanomaterials on stem cells are often separated by narrow concentration margins. Fourth, the mechanistic studies reviewed here are frequently conducted in isolation. Signalling pathways such as p38 MAPK, Wnt/β-catenin, and β1-integrin/TGF-β1 are examined one at a time, whereas in a physiological context these pathways operate in extensive crosstalk. Systematic multi-omics approaches, integrating transcriptomic, proteomic, and epigenomic data from nanomaterial-treated MSCs, will be essential to constructing accurate mechanistic models.

Looking forward, the field is converging on several promising directions. The development of multifunctional nanomaterial platforms, exemplified by carbon quantum dots that combine imaging with differentiation potential, and EV-loaded nanofibers that combine structural scaffolding with sustained biological signalling, represents a conceptual shift from single-function nanomaterials towards integrated theranostic systems capable of simultaneously directing, monitoring, and reporting on stem cell fate in real time. The integration of electroconductive nanomaterials, particularly CNT- and AuNP-based scaffolds, with dynamic electrical stimulation protocols offers a particularly underexplored combinatorial strategy for cardiomyogenic and neurogenic applications. Additionally, the translation of green synthesis methods from laboratory to scalable manufacturing processes will be a prerequisite for clinical-grade nanomaterial production, and represents an area where materials chemistry, process engineering, and regulatory science must converge.

Thus, nanomaterials occupy a central and growing position in stem cell therapy, acting as versatile mediators of differentiation, precision tools for cellular imaging, and increasingly, as multifunctional platforms that unify these roles. The mechanistic diversity uncovered across the five differentiation lineages reflects both the extraordinary range of biological leverage that nanomaterials can exert and the need for lineage-specific, mechanism-informed design principles in their further development. As synthetic methods mature, mechanistic understanding deepens, and in vivo validation progresses, nanomaterials are well positioned to address the central unsolved challenges of stem cell therapy: achieving high-efficiency, selective, and durable lineage commitment in a clinically translatable format.

References

[1] The Insight Partners. (n.d.). Stem cell therapy market trends and forecast by 2031. https://www.theinsightpartners.com/reports/stem-cell-therapy-market

[2] Zhou, X., Yuan, L., Wu, C., Luo, G., Deng, J., & Mao, Z. (2018). Recent review of the effect of nanomaterials on stem cells. RSC Advances, 8(32), 17656–17676. https://doi.org/10.1039/C8RA01483C

[3] Kerativitayanan, P., Carrow, J. K., & Gaharwar, A. K. (2015). Nanomaterials for engineering stem cell responses. Advanced Healthcare Materials, 4(11), 1600–1627. https://doi.org/10.1002/adhm.201500272

[4] Mailänder, V., & Landfester, K. (2009). Interaction of nanoparticles with cells. Biomacromolecules, 10(9), 2379–2400. https://doi.org/10.1021/bm900266r

[5] Wang, Z., Ruan, J., & Cui, D. (2009). Advances and prospect of nanotechnology in stem cells. Nanoscale

Research Letters, 4, 593–605. https://doi.org/10.1007/s11671-009-9292-z

[6] Zhao, F., Zhao, Y., Liu, Y., Chang, X., Chen, C., & Zhao, Y. (2011). Cellular uptake, intracellular trafficking, and cytotoxicity of nanomaterials. Small, 7(10), 1322–1337. https://doi.org/10.1002/smll.201100001

[7] Xia, Y. (2008). Nanomaterials at work in biomedical research. Nature Materials, 7(10), 758–760. https://doi.org/10.1038/nmat2277

[8] Albanese, A., Tang, P. S., & Chan, W. C. W. (2012). The effect of nanoparticle size, shape, and surface chemistry on biological systems. Annual Review of Biomedical Engineering, 14(1), 1–16. https://doi.org/10.1146/annurev-bioeng-071811-150124

[9] Ravichandran, R., Liao, S., Ng, C. C. H., Chan, C. K., Raghunath, M., & Ramakrishna, S. (2009). Effects of nanotopography on stem cell phenotypes. World Journal of Stem Cells, 1(1), 55–66. https://doi.org/10.4252/wjsc.v1.i1.55

[10] Martínez, E., Lagunas, A., Mills, C. A., Rodríguez-Seguí, S., Estévez, M., Oberhansl, S., Comelles, J., & Samitier, J. (2009). Stem cell differentiation by functionalized micro- and nanostructured surfaces. Nanomedicine, 4(1), 65–82. https://doi.org/10.2217/17435889.4.1.65

[11] Ferreira, L., Karp, J. M., Nobre, L., & Langer, R. (2008). New opportunities: The use of nanotechnologies to manipulate and track stem cells. Cell Stem Cell, 3(2), 136–146. https://doi.org/10.1016/j.stem.2008.07.020

[12] Kim, D.-H., Beebe, D. J., & Levchenko, A. (2011). Micro- and nanoengineering for stem cell biology: The promise with a caution. Trends in Biotechnology, 29(8), 399–408. https://doi.org/10.1016/j.tibtech.2011.03.006

[13] McNamara, L. E., McMurray, R. J., Biggs, M. J. P., Kantawong, F., Oreffo, R. O. C., & Dalby, M. J. (2010). Nanotopographical control of stem cell differentiation. Journal of Tissue Engineering, 1(1), 120623. https://doi.org/10.4061/2010/120623

[14] Zhang, L., & Webster, T. J. (2009). Nanotechnology and nanomaterials: Promises for improved tissue regeneration. Nano Today, 4(1), 66–80. https://doi.org/10.1016/j.nantod.2008.10.014

[15] Jasmin, de Souza, G. T., Louzada, R. A., Rosado-de-Castro, P. H., Mendez-Otero, R., & Campos de Carvalho, A. C. (2017). Tracking stem cells with superparamagnetic iron oxide nanoparticles: Perspectives and considerations. International Journal of Nanomedicine, 12, 779–793. https://doi.org/10.2147/IJN.S126530

[16] Kalra, K. T. T. P., & Tomar, P. C. (2014). Stem cell: Basics, classification and applications. American Journal of Phytomedicine and Clinical Therapeutics, 2(7), 919–930.

[17] Strauer, B. E., & Kornowski, R. (2003). Stem cell therapy in perspective. Circulation, 107(7), 929–934. https://doi.org/10.1161/01.CIR.0000057525.13182.24

[18] Francia, V., Montizaan, D., & Salvati, A. (2020). Interactions at the cell membrane and pathways of internalization of nano-sized materials for nanomedicine. Beilstein Journal of Nanotechnology, 11(1), 338–353. https://doi.org/10.3762/bjnano.11.25

[19] Zhang, J., & Jiao, J. (2015). Molecular biomarkers for embryonic and adult neural stem cell and neurogenesis. BioMed Research International, 2015, 727542. https://doi.org/10.1155/2015/727542

[20] Halim, A., Luo, Q., Ju, Y., & Song, G. (2018). A mini review focused on the recent applications of graphene oxide in stem cell growth and differentiation. Nanomaterials, 8(9), 736. https://doi.org/10.3390/nano8090736

[21] Tay, C. Y., Gu, H., Leong, W. S., Yu, H., Li, H. Q., Heng, B. C., Tantang, H., Loo, S. C. J., Li, L. J., & Tan, L. P. (2010). Cellular behavior of human mesenchymal stem cells cultured on single-walled carbon nanotube film. Carbon, 48(4), 1095–1104. https://doi.org/10.1016/j.carbon.2009.11.031

[22] Kam, N. W. S., Jan, E., & Kotov, N. A. (2009). Electrical stimulation of neural stem cells mediated by humanized carbon nanotube composite made with extracellular matrix protein. Nano Letters, 9(1), 273–278. https://doi.org/10.1021/nl802859a

[23] Hung, H. S., Kung, M. L., Chen, F. C., Ke, Y. C., Shen, C. C., Yang, Y. C., Tang, C. M., Yeh, C. A., Hsieh, H. H., & Hsu, S. H. (2021). Nanogold-carried graphene oxide: Anti-inflammation and increased differentiation capacity of mesenchymal stem cells. Nanomaterials, 11(8), 2046. https://doi.org/10.3390/nano11082046

[24] Yim, E. K. F., Pang, S. W., & Leong, K. W. (2007). Synthetic nanostructures inducing differentiation of human mesenchymal stem cells into neuronal lineage. Experimental Cell Research, 313(9), 1820–1829. https://doi.org/10.1016/j.yexcr.2007.02.031

[25] Poudineh, M., Wang, Z., Labib, M., Ahmadi, M., Zhang, L., Das, J., Ahmed, S., Angers, S., & Kelley, S. O. (2018). Three-dimensional nanostructured architectures enable efficient neural differentiation of mesenchymal stem cells via mechanotransduction. Nano Letters, 18(11), 7188–7193. https://doi.org/10.1021/acs.nanolett.8

[26] Baranes, K., Shevach, M., Shefi, O., & Dvir, T. (2016). Gold nanoparticle-decorated scaffolds promote neuronal differentiation and maturation. Nano Letters, 16(5), 2916–2920. https://doi.org/10.1021/acs.nanolett.5b04033

[27] Bhang, S. H., Han, J., Jang, H. K., Noh, M. K., La, W. G., Yi, M., Kim, W. S., Kwon, Y. K., Yu, T., & Kim, B. S. (2015). pH-triggered release of manganese from MnAu nanoparticles that enables cellular neuronal differentiation without cellular toxicity. Biomaterials, 55, 33–43. https://doi.org/10.1016/j.biomaterials.2015.0

[28] Feng, X., & McDonald, J. M. (2011). Disorders of bone remodeling. Annual Review of Pathology: Mechanisms of Disease, 6(1), 121–145. https://doi.org/10.1146/annurev-pathol-011110-130203

[29] Ponzetti, M., & Rucci, N. (2021). Osteoblast differentiation and signaling: Established concepts and emerging topics. International Journal of Molecular Sciences, 22(13), 6651. https://doi.org/10.3390/ijms22136651

[30] Matsuo, K., & Irie, N. (2008). Osteoclast–osteoblast communication. Archives of Biochemistry and Biophysics, 473(2), 201–209. https://doi.org/10.1016/j.abb.2008.03.027

[31] Hadjidakis, D. J., & Androulakis, I. I. (2006). Bone remodeling. Annals of the New York Academy of Sciences, 1092(1), 385–396. https://doi.org/10.1196/annals.1365.035

[32] Urist, M. R. (1965). Bone: Formation by autoinduction. Science, 150(3698), 893–899. https://doi.org/10.1126/science.150.3698.893

[33] Hemmati-Brivanlou, A., & Thomsen, G. H. (1994). Ventral mesodermal patterning in Xenopus embryos: Expression patterns and activities of BMP-2 and BMP-4. Developmental Genetics, 17(1), 78–89. https://doi.org/10.1002/dvg.1020170109

[34] Wozney, J. M., Rosen, V., Celeste, A. J., Mitsock, L. M., Whitters, M. J., Kriz, R. W., Hewick, R. M., & Wang, E. A. (1988). Novel regulators of bone formation: Molecular clones and activities. Science, 242(4885), 1528–1534. https://doi.org/10.1126/science.3201241

[35] Caetano-Lopes, J., Canhão, H., & Fonseca, J. E. (2007). Osteoblasts and bone formation. Acta Reumatológica Portuguesa, 32(2), 103–110.

[36] Li, X., Zhang, Y., Kang, H., Liu, W., Liu, P., Zhang, J., Harris, S. E., & Wu, D. (2005). Sclerostin binds to LRP5/6 and antagonizes canonical Wnt signaling. Journal of Biological Chemistry, 280(20), 19883–19887. https://doi.org/10.1074/jbc.M413274200

[37] Bodine, P. V. N., Zhao, W., Kharode, Y. P., Bex, F. J., Lambert, A.-J., Goad, M. B., Gaur, T., Stein, G. S., Lian, J. B., & Komm, B. S. (2004). The Wnt antagonist secreted frizzled-related protein-1 is a negative regulator of trabecular bone formation in adult mice. Molecular Endocrinology, 18(5), 1222–1237. https://doi.o

[38] Gong, Y., Slee, R. B., Fukai, N., Rawadi, G., Roman-Roman, S., Reginato, A. M., Wang, H., Cundy, T., Glorieux, F. H., Lev, D., Zacharin, M., Oexle, K., Marcelino, J., Suwairi, W., Heeger, S., Sabatakos, G., Apte, S., Adkins, W. N., Allgrove, J., … Warman, M. L. (2001). LDL receptor-related protein 5 (LRP5) affects bone ac

[39] Boyden, L. M., Mao, J., Belsky, J., Mitzner, L., Farhi, A., Mitnick, M. A., Wu, D., Insogna, K., & Lifton, R. P. (2002). High bone density due to a mutation in LDL-receptor–related protein 5. New England Journal of Medicine, 346(20), 1513–1521. https://doi.org/10.1056/NEJMoa013444

[40] Capulli, M., Paone, R., & Rucci, N. (2014). Osteoblast and osteocyte: Games without frontiers. Archives of Biochemistry and Biophysics, 561, 3–12. https://doi.org/10.1016/j.abb.2014.05.003

[41] Liu, H., & Webster, T. J. (2011). Nanomaterials enhance osteogenic differentiation of human mesenchymal stem cells similar to a short peptide of BMP-7. International Journal of Nanomedicine, 6, 2769–2777. https://doi.org/10.2147/IJN.S24493

[42] Mahmoud, N. S., Ahmed, H. H., Mohamed, M. R., Amr, K. S., Aglan, H. A., Ali, M. A. M., & Tantawy, M. A. (2020). Role of nanoparticles in osteogenic differentiation of bone marrow mesenchymal stem cells. Cytotechnology, 72(1), 1–22. https://doi.org/10.1007/s10616-019-00353-y

[43] Yuan, T., Luo, H., Tan, J., Fan, H., & Zhang, X. (2011). The effect of stress and tissue fluid microenvironment on allogeneic chondrocytes in vivo and the immunological properties of engineered cartilage. Biomaterials, 32(26), 6017–6024. https://doi.org/10.1016/j.biomaterials.2011.04.041

[44] Yi, C., Liu, D., Fong, C. C., Zhang, J., & Yang, M. (2010). Gold nanoparticles promote osteogenic differentiation of mesenchymal stem cells through p38 MAPK pathway. ACS Nano, 4(11), 6439–6448. https://doi.org/10.1021/nn101373r

[45] Wang, F. S., Wang, C. J., Sheen-Chen, S. M., Kuo, Y. R., Chen, R. F., & Yang, K. D. (2002). Superoxide mediates shock wave induction of ERK-dependent osteogenic transcription factor (CBFA1) and mesenchymal cell differentiation toward osteoprogenitors. Journal of Biological Chemistry, 277(13), 10931–10937. https://doi.org/

[46] Liu, D., Zhang, J., Yi, C., & Yang, M. (2010). The effects of gold nanoparticles on the proliferation, differentiation, and mineralization function of MC3T3-E1 cells in vitro. Chinese Science Bulletin, 55(9), 1013–1019. https://doi.org/10.1007/s11434-010-0046-1

[47] Khan, J. A., Pillai, B., Das, T. K., Singh, Y., & Maiti, S. (2007). Molecular effects of uptake of gold nanoparticles in HeLa cells. ChemBioChem, 8(11), 1237–1240. https://doi.org/10.1002/cbic.200700165

[48] Verma, A., & Stellacci, F. (2010). Effect of surface properties on nanoparticle–cell interactions. Small, 6(1), 12–21. https://doi.org/10.1002/smll.200901158

[49] Zhang, D., Liu, D., Zhang, J., Fong, C., & Yang, M. (2014). Gold nanoparticles stimulate differentiation and mineralization of primary osteoblasts through the ERK/MAPK signaling pathway. Materials Science and Engineering: C, 42, 70–77. https://doi.org/10.1016/j.msec.2014.04.042

[50] Lee, S. C., Lee, N. H., Patel, K. D., Jang, T.-S., Knowles, J. C., Kim, H.-W., Lee, H.-H., & Lee, J.-H. (2021). The effect of selenium nanoparticles on the osteogenic differentiation of MC3T3-E1 cells. Nanomaterials, 11(2), 557. https://doi.org/10.3390/nano11020557

[51] Xia, Y., Fan, X., Yang, H., Li, L., He, C., Cheng, C., & Haag, R. (2020). ZnO/nanocarbons-modified fibrous scaffolds for stem cell-based osteogenic differentiation. Small, 16(38), 2003010. https://doi.org/10.1002/smll.202003010

[52] Xia, Y., Li, S., Nie, C., Zhang, J., Zhou, S., Yang, H., Li, M., Li, W., Cheng, C., & Haag, R. (2019). A multivalent polyanion-dispersed carbon nanotube toward highly bioactive nanostructured fibrous stem cell scaffolds. Applied Materials Today, 16, 518–528. https://doi.org/10.1016/j.apmt.2019.07.006

[53] Marchesan, S., Kostarelos, K., Bianco, A., & Prato, M. (2015). The winding road for carbon nanotubes in nanomedicine. Materials Today, 18(1), 12–19. https://doi.org/10.1016/j.mattod.2014.07.009

[54] Crowder, S. W., Leonardo, V., Whittaker, T., Papathanasiou, P., & Stevens, M. M. (2016). Material cues as potent regulators of epigenetics and stem cell

function. Cell Stem Cell, 18(1), 39–52. https://doi.org/10.1016/j.stem.2015.12.012

[55] Kim, D.-H., & Wirtz, D. (2015). Cytoskeletal tension induces the polarized architecture of the nucleus. Biomaterials, 48, 161–172. https://doi.org/10.1016/j.biomaterials.2015.01.023

[56] Siqueira, R., Ferreira, J. A., Rizzante, F. A. P., Moura, G. F., Mendonça, D. B. S., de Magalhães, D., Cimões, R., & Mendonça, G. (2021). Hydrophilic titanium surface modulates early stages of osseointegration in osteoporosis. Journal of Periodontal Research, 56(2), 351–362. https://doi.org/10.1111/jre.12826

[57] Ma, Q. L., Zhao, L. Z., Liu, R. R., Jin, B. Q., Song, W., Wang, Y., Zhang, Y. S., Chen, L. H., & Zhang, Y. M. (2014). Improved implant osseointegration of a nanostructured titanium surface via mediation of macrophage polarization. Biomaterials, 35(37), 9853–9867. https://doi.org/10.1016/j.biomaterials.2014.08.025

[58] Brodbeck, W. G., Nakayama, Y., Matsuda, T., Colton, E., Ziats, N. P., & Anderson, J. M. (2002). Biomaterial surface chemistry dictates adherent monocyte/macrophage cytokine expression in vitro. Cytokine, 18(6), 311–319. https://doi.org/10.1006/cyto.2002.1048

[59] Cui, Y., Li, H., Li, Y., & Mao, L. (2022). Novel insights into nanomaterials for immunomodulatory bone regeneration. Nanoscale Advances, 4(2), 334–352. https://doi.org/10.1039/D1NA00741H

[60] Huang, Q., Ouyang, Z., Tan, Y., Wu, H., & Liu, Y. (2019). Activating macrophages for enhanced osteogenic and bactericidal performance by Cu ion release from micro/nano-topographical coating on a titanium substrate. Acta Biomaterialia, 100, 415–426. https://doi.org/10.1016/j.actbio.2019.10.010

[61] Ma, Q. L., Fang, L., Jiang, N., Zhang, L., Wang, Y., Zhang, Y. M., & Chen, L. H. (2018). Bone mesenchymal stem cell secretion of sRANKL/OPG/M-CSF in response to macrophage-mediated inflammatory response influences osteogenesis on nanostructured Ti surfaces. Biomaterials, 154, 234–247. https://doi.org/10.1016/j.biomaterial

[62] Hua, R., Zhao, S., Du, F., & Shu, J. (2024). How mesenchymal stem cells transform into adipocytes: Overview of the current understanding of adipogenic differentiation. World Journal of Stem Cells, 16(3), 281–297. https://doi.org/10.4252/wjsc.v16.i3.281

[63] Lee, W. C., Lim, C. H. Y. X., Shi, H., Tang, L. A. L., Wang, Y., Lim, C. T., & Loh, K. P. (2011). Origin of enhanced stem cell growth and differentiation on graphene and graphene oxide. ACS Nano, 5(9), 7334–7341. https://doi.org/10.1021/nn202190c

[64] Tung, W. L. (2016). Silver nanoparticle based coatings enhance adipogenesis compared to osteogenesis in human mesenchymal stem cells through oxidative stress. NPG Asia Materials.

[65] Kim, J. A., Jang, E. J., Lee, J., Park, J., & Lee, C.-S. (2019). Effects of gold nanostructures on the differentiation of mesenchymal stem cells. Advanced Healthcare Materials, 8(20), e1900310. https://doi.org/10.1002/adhm.201900310

[66] Jingchao Li, Ying Chen, Naoki Kawazoe & Guoping Chen. (2018). Ligand density-dependent influence of arginine–glycine–aspartate functionalised gold nanoparticles on osteogenic and adipogenic differentiation of mesenchymal stem cells. Nano Research, 11(7), 3803–3814. https://doi.org/10.1007/s12274-017-1738-5

[67] Kim, I. S., Cho, T. H., Kim, R., Weber, F. E., & Hwang, S. J. (2011). C/EBP-α and C/EBP-β-mediated adipogenesis of human mesenchymal stem cells using PLGA nanoparticles complexed with poly(ethyleneimine). Biomaterials, 32(33), 8648–8657. https://doi.org/10.1016/j.biomaterials.2011.07.091

[68] Wang, Z., Zheng, Y., Zhao, B., & Zhao, Y. (2017). The negative effect of silica nanoparticles on adipogenic differentiation of human mesenchymal stem cells. RSC Advances, 7(53), 33120–33126. https://doi.org/10.1039/C7RA05671A .

[69] de Crombrugghe, B., Lefebvre, V., & Nakashima, K. (2001). Regulatory mechanisms in the pathways of cartilage and bone formation. Current Opinion in Cell Biology, 13(6), 721–727. https://doi.org/10.1016/S0955-0674(00)00276-3

[70] Park, J. S., Yi, S. W., Kim, H. J., Kim, S. M., Kim, J.-H., & Park, K.-H. (2017). Construction of PLGA nanoparticles coated with polycistronic SOX5, SOX6, and SOX9 genes for chondrogenesis of human mesenchymal stem cells. ACS Applied Materials & Interfaces, 9(2), 1361–1372. https://doi.org/10.1021/acsami.6b15354

[71] Carballo-Pedrares, N., Sanjurjo-Rodriguez, C., Señarís, J., Díaz-Prado, S., & Rey-Rico, A. (2022). Chondrogenic differentiation of human mesenchymal stem cells via SOX9 delivery in cationic niosomes. Pharmaceutics, 14(11), 2327. https://doi.org/10.3390/pharmaceutics14112327

[72] Zhao, M., Gao, X., Wei, J., Tu, C., Zheng, H., Jing, K., Chu, J., Ye, W., & Groth, T. (2022). Chondrogenic differentiation of mesenchymal stem cells through cartilage matrix-inspired surface coatings. Frontiers in Bioengineering and Biotechnology, 10, 991855. https://doi.org/10.3389/fbioe.2022.991855

[73] Casanova, M. R., Osório, H., Reis, R. L., Martins, A., & Neves, N. M. (2021). Chondrogenic differentiation induced by extracellular vesicles bound to a nanofibrous substrate. Npj Regenerative Medicine, 6(1), 79. https://doi.org/10.1038/s41536-021-00190-8

[74] Doppler, S. A., Carvalho, C., Lahm, H., Deutsch, M.-A., Dreßen, M., Puluca, N., Lange, R., & Krane, M. (2017). Cardiac fibroblasts: More than mechanical support. Journal of Thoracic Disease, 9(Suppl 1), S36–S51. https://doi.org/10.21037/jtd.2017.03.122

[75] Sun, H., Mou, Y., Li, Y., Li, X., Chen, Z., Duval, K., Huang, Z., Dai, R., Tang, L., & Tian, F. (2016). Carbon nanotube-based substrates promote cardiogenesis in brown adipose-derived stem cells via β1-integrin-dependent TGF-β1 signaling pathway. International Journal of Nanomedicine, 11, 4381–4395. https://doi.org/10.21

[76] Wickham, A. M., Islam, M. M., Mondal, D., Phopase, J., Sadhu, V., Tamás, É., Polisetti, N., Richter-Dahlfors, A., Liedberg, B., & Griffith, M. (2014).

Polycaprolactone–thiophene-conjugated carbon nanotube meshes as scaffolds for cardiac progenitor cells. Journal of Biomedical Materials Research Part B: Applied Biomateria

[77] Ravichandran, R., Sridhar, R., Venugopal, J. R., Sundarrajan, S., Mukherjee, S., & Ramakrishna, S. (2014). Gold nanoparticle loaded hybrid nanofibers for cardiogenic differentiation of stem cells for infarcted myocardium regeneration. Macromolecular Bioscience, 14(4), 515–525. https://doi.org/10.1002/mabi.201300407

[78] Mohammadi Amirabad, L., Massumi, M., Shamsara, M., Shabani, I., Amari, A., Mossahebi-Mohammadi, M., Hosseinzadeh, S., Vakilian, S., Steinbach, S. K., Khorramizadeh, M. R., Soleimani, M., & Barzin, J. (2021). Silver nanoparticles induce the cardiomyogenic differentiation of bone marrow derived mesenchymal stem cells via t

[79] Solanki, A., Kim, J. D., & Lee, K.-B. (2008). Nanotechnology for regenerative medicine: Nanomaterials for stem cell imaging. Nanomedicine, 3(4), 567–578. https://doi.org/10.2217/17435889.3.4.567

[80] Bulte, J. W. M., & Kraitchman, D. L. (2004). Iron oxide MR contrast agents for molecular and cellular imaging. NMR in Biomedicine, 17(7), 484–499. https://doi.org/10.1002/nbm.924

[81] Dutz, S., Andrä, W., Hergt, R., Müller, R., Oestreich, C., Schmidt, C., Töpfer, J., & Bellemann, M. E. (2007). Influence of dextran coating on the magnetic behaviour of iron oxide nanoparticles. Journal of Magnetism and Magnetic Materials, 311(1), 51–54. https://doi.org/10.1016/j.jmmm.2006.11.178

[82] Lawaczeck, R., Menzel, M., & Pietsch, H. (2004). Superparamagnetic iron oxide particles: Contrast media for magnetic resonance imaging. Applied Organometallic Chemistry, 18(10), 506–513. https://doi.org/10.1002/aoc.715

[83] Castaneda, R. T., Khurana, A., Khan, R., & Daldrup-Link, H. E. (2011). Labeling stem cells with ferumoxytol, an FDA-approved iron oxide nanoparticle. Journal of Visualized Experiments, (57), e3482. https://doi.org/10.3791/3482

[84] Wang, Y., & Hu, A. (2014). Carbon quantum dots: Synthesis, properties and applications. Journal of Materials Chemistry C, 2(34), 6921–6939. https://doi.org/10.1039/C4TC00988F

[85] Lin, L., Luo, Y., Tsai, P., Wang, J., & Chen, X. (2018). Metal ion doped carbon quantum dots: Synthesis, physicochemical properties, and their applications. TrAC Trends in Analytical Chemistry, 103, 87–101. https://doi.org/10.1016/j.trac.2018.03.015

[86] Teradal, N. L., & Jelinek, R. (2017). Carbon nanomaterials in biological studies and biomedicine. Advanced Healthcare Materials, 6(17), 1700574. https://doi.org/10.1002/adhm.201700574

[87] Sun, Y., Zhang, M., Bhandari, B., & Yang, C. (2022). Recent development of carbon quantum dots: Biological toxicity, antibacterial properties and application in foods. Food Reviews International, 38(7), 1513–1532. https://doi.org/10.1080/87559129.2020.1870035

[88] Majood, M., Garg, P., Chaurasia, R., Agarwal, A., Mohanty, S., & Mukherjee, M. (2022). Carbon quantum dots for stem cell imaging and deciding the fate of stem cell differentiation. ACS Omega, 7(33), 28685–28693. https://doi.org/10.1021/acsomega.2c02572

[89] Huang, C., Dong, H., Su, Y., Wu, Y., Narron, R., & Yong, Q. (2019). Synthesis of carbon quantum dot nanoparticles derived from byproducts in bio-refinery process for cell imaging and in vivo bioimaging. Nanomaterials, 9(3), 387. https://doi.org/10.3390/nano9030387

[90] Wang, J., Li, Q., Zhou, J., Wang, Y., Yu, L., Peng, H., & Zhu, J. (2017). Synthesis, characterization and cells and tissues imaging of carbon quantum dots. Optical Materials, 72, 15–19. https://doi.org/10.1016/j.optmat.2017.05.034

[91] Hsieh, S.-C., Wang, F.-F., Lin, C.-S., Chen, Y.-J., Hung, S.-C., & Wang, Y.-J. (2006). The inhibition of osteogenesis with human bone marrow mesenchymal stem cells by CdSe/ZnS quantum dot labels. Biomaterials, 27(8), 1656–1664. https://doi.org/10.1016/j.biomaterials.2005.09.004

[92] Liu, C., & Zhang, N. (2011). Nanoparticles in gene therapy: Principles, prospects, and challenges. Progress in Molecular Biology and Translational Science, 104, 509–562. https://doi.org/10.1016/B978-0-12-416020-0.00013-9

[93] Seleverstov, O., Zabirnyk, O., Zscharnack, M., Bulavina, L., Nowicki, M., Heinrich, J.-M., Yezhelyev, M., Emmrich, F., O'Regan, R., & Bader, A. (2006). Quantum dots for human mesenchymal stem cells labeling: A size-dependent autophagy activation. Nano Letters, 6(12), 2826–2832. https://doi.org/10.1021/nl0619711

[94] Kikuchi, A., Aoki, Y., Sugaya, S., Serikawa, T., Takakuwa, K., Tanaka, K., Suzuki, N., & Kikuchi, H. (1999). Development of novel cationic liposomes for efficient gene transfer into peritoneal disseminated tumor. Human Gene Therapy, 10(6), 947–955. https://doi.org/10.1089/10430349950018384

[95] Papadimitriou, S. A., Robin, M. P., Ceric, D., O'Reilly, R. K., Marino, S., & Resmini, M. (2016). Fluorescent polymeric nanovehicles for neural stem cell modulation. Nanoscale, 8(39), 17340–17349. https://doi.org/10.1039/C6NR05717C

[96] ur Rehman, Z., Zuhorn, I. S., & Hoekstra, D. (2013). How cationic lipids transfer nucleic acids into cells and across cellular membranes: Recent advances. Journal of Controlled Release, 166(1), 46–56. https://doi.org/10.1016/j.jconrel.2012.12.014

[97] Chen, D., Li, Q., Meng, Z., Guo, L., Tang, Y., Liu, Z., Gu, Y., Sun, X., Bhattacharya, S., Liu, W., & Wu, C. (2017). Bright polymer dots tracking stem cell engraftment and migration to injured mouse liver. Theranostics, 7(7), 1820–1834. https://doi.org/10.7150/thno.18614

[98] Betancourt, T., Byrne, J. D., Sunaryo, N., Crowder, S. W., Kadapakkam, M., Patel, S., Casciato, S., & Brannon-Peppas, L. (2009). PEGylation strategies for active targeting of PLA/PLGA nanoparticles. Journal of Biomedical Materials Research Part A, 91(1), 263–276. https://doi.org/10.1002/jbm.a.32247

[99] James, M. L., & Gambhir, S. S. (2012). A molecular imaging primer: Modalities, imaging agents, and applications. Physiological Reviews, 92(2), 897–965. https://doi.org/10.1152/physrev.00049.2010

[100] Lü, J. M., Wang, X., Marin-Muller, C., Wang, H., Lin, P. H., Yao, Q., & Chen, C. (2009). Current advances in research and clinical applications of PLGA-based nanotechnology. Expert Review of Molecular Diagnostics, 9(4), 325–341. https://doi.org/10.1586/erm.09.15

[101] Keles, E., Song, Y., Du, D., Dong, W.-J., & Lin, Y. (2016). Recent progress in nanomaterials for gene delivery applications. Biomaterials Science, 4(9), 1291–1309. https://doi.org/10.1039/C6BM00441E

[102] Zhou, X., Zheng, Q., Wang, C., Xu, J., Wu, J.-P., Kirk, T. B., Ma, D., & Xue, W. (2016). Star-shaped amphiphilic hyperbranched polyglycerol conjugated with dendritic poly(L-lysine) for the codelivery of docetaxel and MMP-9 siRNA in cancer therapy. ACS Applied Materials & Interfaces, 8(20), 12609–12619. https://doi.org/10.

[103] Ghosh, S. K., Nandi, S. K., Kundu, B., Datta, S., De, D. K., Roy, S. K., & Basu, D. (2011). Synthesis of nano-sized hydroxyapatite powders through solution combustion route under different reaction conditions. Materials Science and Engineering: B, 176(1), 14–21. https://doi.org/10.1016/j.mseb.2010.08.008

[104] Fujishiro, Y., Yabuki, H., Kawamura, K., Sato, T., & Okuwaki, A. (1993). Preparation of needle-like hydroxyapatite by homogeneous precipitation under hydrothermal conditions. Journal of Chemical Technology & Biotechnology, 57(4), 349–353. https://doi.org/10.1002/jctb.280570409

[105] Yeong, K. C. B., Wang, J., & Ng, S. C. (2001). Mechanochemical synthesis of nanocrystalline hydroxyapatite from CaO and CaHPO4. Biomaterials, 22(20), 2705–2712. https://doi.org/10.1016/S0142-9612(01)00013-0

[106] Wang, H., Eliaz, N., & Hobbs, L. W. (2011). The nanostructure of an electrochemically deposited hydroxyapatite coating. Materials Letters, 65(15–16), 2455–2457. https://doi.org/10.1016/j.matlet.2011.04.102

[107] Kaygili, O., Keser, S., Al-Orainy, R. H., Ates, T., & Yakuphanoglu, F. (2014). In vitro characterization of polyvinyl alcohol assisted hydroxyapatite derived by sol-gel method. Materials Science and Engineering: C, 35, 239–244. https://doi.org/10.1016/j.msec.2013.11.009

[108] Wang, P., Li, C., Gong, H., Jiang, X., Wang, H., & Li, K. (2010). Effects of synthesis conditions on the morphology of hydroxyapatite nanoparticles produced by wet chemical process. Powder Technology, 203(2), 315–321. https://doi.org/10.1016/j.powtec.2010.05.023

[109] Wijesinghe, W. P. S. L., Mantilaka, M. M. M. G. P. G., Premalal, E. V. A., Herath, H. M. T. U., Mahalingam, S., Edirisinghe, M., Rajapakse, R. P. V. J., & Rajapakse, R. M. G. (2014). Facile synthesis of both needle-like and spherical hydroxyapatite nanoparticles: Effect of synthetic temperature and calcination on morpholo

[110] Elbasuney, S. (2020). Green synthesis of hydroxyapatite nanoparticles with controlled morphologies and surface properties toward biomedical applications. Journal of Inorganic and Organometallic Polymers and Materials, 30(3), 899–906. https://doi.org/10.1007/s10904-019-01247-4

[111] Vinayagam, R., Kandati, S., Murugesan, G., Goveas, L. C., Baliga, A., Pai, S., Varadavenkatesan, T., Kaviyarasu, K., & Selvaraj, R. (2023). Bioinspiration synthesis of hydroxyapatite nanoparticles using eggshells as a calcium source: Evaluation of Congo red dye adsorption potential. Journal of Materials Research and Techn

[112] Liu, H., & Webster, T. J. (2010). Mechanical properties of dispersed ceramic nanoparticles in polymer composites for orthopedic applications. International Journal of Nanomedicine, 5, 299–313. https://doi.org/10.2147/IJN.S9089

[113] Teimouri, M., Khosravi-Nejad, F., Attar, F., Saboury, A. A., Kostova, I., Benelli, G., & Falahati, M. (2018). Gold nanoparticles fabrication by plant extracts: Synthesis, characterization, degradation of 4-nitrophenol from industrial wastewater, and insecticidal activity – A review. Journal of Cleaner Production, 184, 740

[114] Mourato, A., Gadanho, M., Lino, A. R., & Tenreiro, R. (2011). Biosynthesis of crystalline silver and gold nanoparticles by extremophilic yeasts. Bioinorganic Chemistry and Applications, 2011, 546074. https://doi.org/10.1155/2011/546074

[115] Roychoudhury, A. (2020). Yeast-mediated green synthesis of nanoparticles for biological applications. Indian Journal of Pharmaceutical and Biological Research, 8(3), 26–31.

[116] Syed, A., & Ahmad, A. (2012). Extracellular biosynthesis of platinum nanoparticles using the fungus Fusarium oxysporum. Colloids and Surfaces B: Biointerfaces, 97, 27–31. https://doi.org/10.1016/j.colsurfb.2012.03.026

[117] Singh, P., Kim, Y.-J., Zhang, D., & Yang, D.-C. (2016). Biological synthesis of nanoparticles from plants and microorganisms. Trends in Biotechnology, 34(7), 588–599. https://doi.org/10.1016/j.tibtech.2016.02.006

[118] Chatterjee, S., Mahanty, S., Das, P., Chaudhuri, P., & Das, S. (2020). Biofabrication of iron oxide nanoparticles using manglicolous fungus Aspergillus niger BSC-1 and removal of Cr(VI) from aqueous solution. Chemical Engineering Journal, 385, 123790. https://doi.org/10.1016/j.cej.2019.123790

[119] Balaji, D. S., Basavaraja, S., Deshpande, R., Mahesh, D. B., Prabhakar, B. K., & Venkataraman, A. (2009). Extracellular biosynthesis of functionalized silver nanoparticles by strains of Cladosporium cladosporioides fungus. Colloids and Surfaces B: Biointerfaces, 68(1), 88–92. https://doi.org/10.1016/j.colsurfb.2008.09.022

[120] Olvera-Aripez, J., Camacho-López, S., Flores-Castañeda, M., López-Morales, C. A., Flores-García, M., Ocampo-García, B., & González-González, R. (2024). Biosynthesis of gold nanoparticles by fungi and its potential in SERS. Bioprocess and Biosystems Engineering, 47, 1191–1203. https://doi.org/10.1007/s00449-024-03053-w

[121] Frisvad, J. C. (2012). Media and growth conditions for induction of secondary metabolite production. In A. Zeilinger (Ed.), Fungal secondary metabolism: Methods and protocols (pp. 47–58). Humana Press. https://doi.org/10.1007/978-1-62703-122-6_3

[122] Chakraborty, N., Banerjee, J., Chakraborty, P., Banerjee, A., Chanda, S., Ray, K., Acharya, K., & Sarkar, J. (2022). Green synthesis of copper/copper oxide nanoparticles and their applications: A review. Green Chemistry Letters and Reviews, 15(1), 187–215. https://doi.org/10.1080/17518253.2022.2027487

[123] Bogireddy, N. K. R., Anand, K. K. H., & Mandal, B. K. (2015). Gold nanoparticles—synthesis by Sterculia acuminata extract and its catalytic efficiency in alleviating different organic dyes. Journal of Molecular Liquids, 211, 868–875. https://doi.org/10.1016/j.molliq.2015.08.010

[124] Islam, N. U., Jalil, K., Shahid, M., Rauf, A., Muhammad, N., Khan, A., Shah, M. R., & Khan, M. A. (2019). Green synthesis and biological activities of gold nanoparticles functionalized with Salix alba. Arabian Journal of Chemistry, 12(8), 2914–2925. https://doi.org/10.1016/j.arabjc.2015.06.025

[125] Vijayashree, I., Niranjana, P., Prabhu, G., Sureshbabu, V. V., & Manjanna, J. (2017). Conjugation of Au nanoparticles with chlorambucil for improved anticancer activity. Journal of Cluster Science, 28(1), 133–148. https://doi.org/10.1007/s10876-016-1053-4

[126] Lee, K. X., Shameli, K., Yew, Y. P., Teow, S.-Y., Jahangirian, H., Rafiee-Moghaddam, R., & Webster, T. J. (2020). Recent developments in the facile bio-synthesis of gold nanoparticles (AuNPs) and their biomedical applications. International Journal of Nanomedicine, 15, 275–300. https://doi.org/10.2147/IJN.S233966

[127] Yu, J., Xu, D., Guan, H. N., Wang, C., & Huang, L. K. (2016). Facile one-step green synthesis of gold nanoparticles using Citrus maxima aqueous extracts and its catalytic activity. Materials Letters, 166, 110–112. https://doi.org/10.1016/j.matlet.2015.12.031

[128] Ghodake, G., & Lee, D. S. (2011). Green synthesis of gold nanostructures using pear extract as effective reducing and coordinating agent. Korean Journal of Chemical Engineering, 28(12), 2329–2335. https://doi.org/10.1007/s11814-011-0115-4

[129] Flohé, L. (2009). The labour pains of biochemical selenology: The history of selenoprotein biosynthesis. Biochimica et Biophysica Acta – General Subjects, 1790(11), 1389–1403. https://doi.org/10.1016/j.bbagen.2009.03.031

[130] Chaudhary, S., Umar, A., & Mehta, S. K. (2016). Selenium nanomaterials: An overview of recent developments in synthesis, properties and potential applications. Progress in Materials Science, 83, 270–329. https://doi.org/10.1016/j.pmatsci.2016.07.001

[131] Underwood, E. J. (1977). Trace elements in human and animal nutrition (4th ed.). Academic Press.

[132] Mahmoodi, S. R., Bayati, M., Rad, S. H., Heidari, E. K., Foroumadi, A., & Gilani, K. (2013). Dielectrophoretic trapping of selenium nanorods for use in device applications. Journal of Materials Science: Materials in Electronics, 24, 4554–4559. https://doi.org/10.1007/s10854-013-1436-y

[133] Kumar, N., Kumar, R., Kumar, S., & Chakarvarti, S. K. (2014). Microstructural, optical and electrical investigations of large scale selenium nanowires prepared by template electrodeposition. Journal of Materials Science: Materials in Electronics, 25, 3537–3542. https://doi.org/10.1007/s10854-014-2050-3

[134] Xi, G., Xiong, K., Zhao, Q., Zhang, R., Zhang, H., & Qian, Y. (2006). Nucleation–dissolution–recrystallization: A new growth mechanism for t-selenium nanotubes. Crystal Growth & Design, 6(2), 577–582. https://doi.org/10.1021/cg050481d

[135] Tran, P. A., O'Brien-Simpson, N., Reynolds, E. C., Pantarat, N., Biswas, D. P., & O'Connor, A. J. (2016). Low cytotoxic trace element selenium nanoparticles and their differential antimicrobial properties against S. aureus and E. coli. Nanotechnology, 27(4), 045101. https://doi.org/10.1088/0957-4484/27/4/045101

[136] Ionin, A. A., Ivanova, A. K., Khmel'nitskii, R. A., Klevkov, Y. V., Kudryashov, S. I., Levchenko, A. O., Mel'nik, N. N., Nastulyavichus, A. A., Saraeva, I. N., & Tolordava, E. R. (2018). Antibacterial effect of the laser-generated Se nanocoatings on Staphylococcus aureus and Pseudomonas aeruginosa biofilms. Laser Physics

[137] Tran, P. A., & Webster, T. J. (2011). Selenium nanoparticles inhibit Staphylococcus aureus growth. International Journal of Nanomedicine, 6, 1553–1558. https://doi.org/10.2147/IJN.S21729

[138] Guisbiers, G., Wang, Q., Khachatryan, E., Mimun, L. C., Mendoza-Cruz, R., Larese-Casanova, P., Webster, T. J., & Nash, K. L. (2016). Inhibition of E. coli and S. aureus with selenium nanoparticles synthesized by pulsed laser ablation in deionized water. International Journal of Nanomedicine, 11, 3731–3736. https://doi.org

[139] Shoeibi, S., & Mashreghi, M. (2017). Biosynthesis of selenium nanoparticles using Enterococcus faecalis and evaluation of their antibacterial activities. Journal of Trace Elements in Medicine and Biology, 39, 135–139. https://doi.org/10.1016/j.jtemb.2016.09.003

[140] Cremonini, E., Boaretti, M., Vandecandelaere, I., Zonaro, E., Coenye, T., Lleò, M. M., Bernardi, P., Zanoni, S., & Vallini, G. (2018). Biogenic selenium nanoparticles synthesized by Stenotrophomonas maltophilia Se ITE02 loose antibacterial and antibiofilm efficacy as a result of the progressive alteration of their organic

[141] Al Jahdaly, B. A., Al-Radadi, N. S., Eldin, G. M., Almahri, A., Ahmed, M., Shoueir, K., & Janowska, I. (2021). Selenium nanoparticles synthesized using an eco-friendly method: Dye decolorization from aqueous solutions, cell viability, antioxidant, and antibacterial effectiveness. Journal of Materials Research and Technolo

[142] Shar, A. H., Lakhan, M. N., Wang, J., Ahmed, M., Alali, K. T., Ahmed, R., Bhutto, A. B., Shar, A. H., Chandio, A. D., & Dayo, A. Q. (2019). Facile synthesis and characterization of selenium nanoparticles by the hydrothermal approach. Digest Journal of Nanomaterials and Biostructures, 14(3), 867–872.

[143] Menon, S., Devi, K. S. S., Agarwal, H., & Shanmugam, V. K. (2019). Efficacy of biogenic selenium nanoparticles from an extract of ginger

towards evaluation on anti-microbial and anti-oxidant activities. Colloid and Interface Science Communications, 29, 1–8. https://doi.org/10.1016/j.colcom.2018.12.004

[144] Fan, D., Li, L., Li, Z., Zhang, Y., Ma, X., Wu, L., Ma, Z., Guo, Y., & Guo, F. (2020). Biosynthesis of selenium nanoparticles and their protective, antioxidative effects in streptozotocin induced diabetic rats. Science and Technology of Advanced Materials, 21(1), 505–514. https://doi.org/10.1080/14686996.2020.1786927

[145] Ramamurthy, C. H., Sampath, K. S., Arunkumar, P., Kumar, M. S., Sujatha, V., Premkumar, K., & Thirunavukkarasu, C. (2013). Green synthesis and characterization of selenium nanoparticles and its augmented cytotoxicity with doxorubicin on cancer cells. Bioprocess and Biosystems Engineering, 36, 1131–1139. https://doi.org/10

[146] Nguyen, T. H., Vardhanabhuti, B., Lin, M., & Mustapha, A. (2017). Antibacterial properties of selenium nanoparticles and their toxicity to Caco-2 cells. Food Control, 77, 17–24. https://doi.org/10.1016/j.foodcont.2017.01.018

[147] Jiang, F., Cai, W., & Tan, G. (2017). Facile synthesis and optical properties of small selenium nanocrystals and nanorods. Nanoscale Research Letters, 12, 536. https://doi.org/10.1186/s11671-017-2313-y

[148] Mikhailova, E. O. (2023). Selenium nanoparticles: Green synthesis and biomedical application. Molecules, 28(24), 8125. https://doi.org/10.3390/molecules28248125

[149] Ho, C. T., Nguyen, T. H., Lam, T. T., Le, D. Q., Nguyen, C. X., Lee, J. H., & Hur, H.-G. (2021). Biogenic synthesis of selenium nanoparticles by Shewanella sp. HN-41 using a modified bioelectrochemical system. Electronic Journal of Biotechnology, 54, 1–7. https://doi.org/10.1016/j.ejbt.2021.08.001

[150] Hu, D., Yu, S., Yu, D., Liu, N., Tang, Y., Fan, Y., Wang, C., & Wu, A. (2019). Biogenic Trichoderma harzianum-derived selenium nanoparticles with control functionalities originating from diverse recognition metabolites against phytopathogens and mycotoxins. Food Control, 106, 106748. https://doi.org/10.1016/j.foodcont.201

[151] Vyas, J., & Rana, S. (2018). Synthesis of selenium nanoparticles using Allium sativum extract and analysis of their antimicrobial property against gram positive bacteria. Pharma Innovation, 7(4), 262–266.

[152] Vetchinkina, E., Loshchinina, E., Kursky, V., & Nikitina, V. (2013). Reduction of organic and inorganic selenium compounds by the edible medicinal basidiomycete Lentinula edodes and the accumulation of elemental selenium nanoparticles in its mycelium. Journal of Microbiology, 51, 829–835. https://doi.org/10.1007/s12275-01

[153] Cittrarasu, V., Kaliannan, D., Dharman, K., Maluventhen, V., Easwaran, M., Liu, W. C., Balasubramanian, B., & Arumugam, M. (2021). Green synthesis of selenium nanoparticles mediated from Ceropegia bulbosa Roxb extract and its cytotoxicity, antimicrobial, mosquitocidal and photocatalytic activities. Scientific Reports, 11(

[154] Puri, A., & Patil, S. (2022). Tinospora cordifolia stem extract-mediated green synthesis of selenium nanoparticles and its biological applications. Pharmacognosy Research, 14(3), 326–333. https://doi.org/10.5530/pres.14.3.46

[155] Akçay, F. A., & Avcı, A. (2020). Effects of process conditions and yeast extract on the synthesis of selenium nanoparticles by a novel indigenous isolate Bacillus sp. EKT1 and characterization of nanoparticles. Archives of Microbiology, 202(8), 2233–2243. https://doi.org/10.1007/s00203-020-01940-2

[156] Aldeen, T. S., Ahmed Mohamed, H. E., & Maaza, M. (2021). ZnO nanoparticles prepared via a green synthesis approach: Physical properties, photocatalytic and antibacterial activity. Journal of Physics and Chemistry of Solids, 160, 110313. https://doi.org/10.1016/j.jpcs.2021.110313

[157] Huang, W., Tao, F., Li, F., Mortimer, M., & Guo, L.-H. (2021). Antibacterial nanomaterials for environmental and consumer product applications. NanoImpact, 20, 100268. https://doi.org/10.1016/j.impact.2020.100268

[158] Rambabu, K., Bharath, G., Banat, F., & Show, P. L. (2021). Green synthesis of zinc oxide nanoparticles using Phoenix dactylifera waste as bioreductant for effective dye degradation and antibacterial performance in wastewater treatment. Journal of Hazardous Materials, 402, 123560. https://doi.org/10.1016/j.jhazmat.2020.123

[159] Chauhan, A., Verma, R., Kumari, S., Sharma, A., Shandilya, P., Li, X., Batoo, K. M., Imran, A., Kulshrestha, S., & Kumar, R. (2020). Photocatalytic dye degradation and antimicrobial activities of pure and Ag-doped ZnO using Cannabis sativa leaf extract. Scientific Reports, 10(1), 7881. https://doi.org/10.1038/s41598-020-6

[160] Mintcheva, N., Aljulaih, A. A., Wunderlich, W., Kulinich, S. A., & Iwamori, S. (2018). Laser-ablated ZnO nanoparticles and their photocatalytic activity toward organic pollutants. Materials, 11(7), 1127. https://doi.org/10.3390/ma11071127

[161] Hashmi, M. S. J. (Ed.). (2014). Comprehensive materials processing. Elsevier.

[162] Hasnidawani, J. N., Azlina, H. N., Norita, H., Bonnia, N. N., Ratim, S., & Ali, E. S. (2016). Synthesis of ZnO nanostructures using sol-gel method. Procedia Chemistry, 19, 211–216. https://doi.org/10.1016/j.proche.2016.03.095

[163] Mishra, S. K., Srivastava, R. K., Prakash, S. G., Yadav, R. S., & Panday, A. C. (2010). Photoluminescence and photoconductive characteristics of hydrothermally synthesized ZnO nanoparticles. Opto-Electronics Review, 18(4), 467–473. https://doi.org/10.2478/s11772-010-0047-z

[164] Inoguchi, M., Suzuki, K., Kageyama, K., Takagi, H., & Sakabe, Y. (2008). Monodispersed and well-crystallized zinc oxide nanoparticles fabricated by microemulsion method. Journal of the American Ceramic Society, 91(12), 3850–3855. https://doi.org/10.1111/j.1551-2916.2008.02724.x

[165] Perveen, R., Shujaat, S., Qureshi, Z., Nawaz, S., Khan, M. I., & Iqbal, M. (2020). Green versus sol-gel synthesis of ZnO nanoparticles and antimicrobial

activity evaluation against panel of pathogens. Journal of Materials Research and Technology, 9(4), 7817–7827. https://doi.org/10.1016/j.jmrt.2020.04.089

[166] Gawade, V. V., Gavade, N. L., Shinde, H. M., Babar, S. B., Kadam, A. N., & Garadkar, K. M. (2017). Green synthesis of ZnO nanoparticles by using Calotropis procera leaves for the photodegradation of methyl orange. Journal of Materials Science: Materials in Electronics, 28, 14033–14039. https://doi.org/10.1007/s10854-017-7

[167] Thi, T. U. D., Nguyen, T. T., Thi, Y. D., Thi, K. H. T., Phan, B. T., & Pham, K. N. (2020). Green synthesis of ZnO nanoparticles using orange fruit peel extract for antibacterial activities. RSC Advances, 10(40), 23899–23907. https://doi.org/10.1039/D0RA04926C

[168] Rao, R., Pint, C. L., Islam, A. E., Weatherup, R. S., Hofmann, S., Meshot, E. R., Wu, F., Zhou, C., Dee, N., Amama, P. B., Carpena-Nuñez, J., Shi, W., Plata, D. L., Penev, E. S., Yakobson, B. I., Balbuena, P. B., Bichara, C., Futaba, D. N., Noda, S., … Harutyunyan, A. R. (2018). Carbon nanotubes and related nanomaterials:

[169] Danafar, F., Fakhru'l-Razi, A., Salleh, M. A. M., & Biak, D. R. A. (2009). Fluidised bed catalytic chemical vapour deposition synthesis of carbon nanotubes — A review. Chemical Engineering Journal, 155(1–2), 37–48. https://doi.org/10.1016/j.cej.2009.07.052

[170] Suriani, A. B., Azira, A. A., Nik, S. F., Md Nor, R., & Rusop, M. (2009). Synthesis of vertically aligned carbon nanotubes using the chemical vapour deposition method with a camphor precursor and iron catalyst. Materials Letters, 63(27), 2339–2341. https://doi.org/10.1016/j.matlet.2009.07.068

[171] Islam, S. S., Khan, M. S., Nema, A. K., Agarwal, R., & Gupta, P. (2017). Synthesis of carbon nanotubes using green plant extract as catalyst: Unconventional concept and its realization. Applied Nanoscience, 7(8), 835–842. https://doi.org/10.1007/s13204-017-0598-3

[172] Duraia, E. M., Mansurov, Z., & Beall, G. W. (2024). Efficient eco-friendly synthesis of carbon nanotubes over graphite nanosheets from yellow corn: A one-step green approach. Scientific Reports, 14, 16399. https://doi.org/10.1038/s41598-024-65893-6

[173] Alhajri, H. M., Al-Batty, S., Almurshedi, A. S., & Alotaibi, H. F. (2022). Olive leaf extracts for a green synthesis of silver-functionalized multi-walled carbon nanotubes. Journal of Functional Biomaterials, 13(4), 224. https://doi.org/10.3390/jfb13040224

[174] Novoselov, K. S., Geim, A. K., Morozov, S. V., Jiang, D., Zhang, Y., Dubonos, S. V., Grigorieva, I. V., & Firsov, A. A. (2004). Electric field effect in atomically thin carbon films. Science, 306(5696), 666–669. https://doi.org/10.1126/science.1102896

[175] Abdullah, N. H., Shameli, K., Abdullah, E. C., & Abdullah, L. C. (2020). Green and low-cost approach for graphene oxide reduction using natural plant extracts. Materials Today: Proceedings, 31, A1–A10. https://doi.org/10.1016/j.matpr.2020.09.232

[176] Suryawanshi, S. R., Warule, S. S., Patil, S. S., Patil, K. R., & More, M. A. (2016). Studies on synthesis of reduced graphene oxide (RGO) via green route and its electrical property. Materials Today: Chemistry, 1–2, 1–9. https://doi.org/10.1016/j.mtchem.2016.11.003

[177] Kumar, P., Bangwal, D., Anand, S., Nisha, Bhatt, M. D., & Singhal, M. (2018). Green eco-friendly pathway for the synthesis of reduced graphene oxide using extract of Tagetes erecta (marigold flower). International Journal of Modern Physics B, 32(20), 1840068. https://doi.org/10.1142/S0217979218400684

[178] Pandiyan, R., Latha, N., Jothivenkatachalam, K., & Prabhu, S. (2024). An efficient and green strategy for the synthesis of graphene with aqueous polyphenol extracts of orchid flower (Dendrobium anosmum) for charge storage. Journal of Alloys and Compounds, 945, 169248. https://doi.org/10.1016/j.jallcom.2024.169248

[179] Deivanathan, G., Arockia Doss, M. X., Ananth, A., & Rajan, M. (2024). Green synthesis of reduced graphene oxide using the Tinospora cordifolia plant extract. ACS Omega, 9(14), 15898–15910. https://doi.org/10.1021/acsomega.4c00748